

Ensemble-Embedding Graph Neural Network for Direct Prediction of Optical Spectra from Crystal Structures

Nguyen Tuan Hung* Ryotaro Okabe Abhijatmedhi Chotrattanapituk Mingda Li*

Prof. N. T. H.

Frontier Research Institute for Interdisciplinary Sciences, Tohoku University, Sendai 980-8578, Japan
Quantum Measurement Group, MIT, Cambridge, MA 02139-4307, USA

Email Address: nguyen.tuan.hung.e4@tohoku.ac.jp

R. O.

Department of Chemistry, MIT, Cambridge, MA 02139-4307, USA
Quantum Measurement Group, MIT, Cambridge, MA 02139-4307, USA

A. C.

Department of Electrical Engineering and Computer Science, MIT, Cambridge, MA 02139-4307, USA
Quantum Measurement Group, MIT, Cambridge, MA 02139-4307, USA

Prof. M. L.

Department of Nuclear Science and Engineering, MIT, Cambridge, MA 02139-4307, USA
Quantum Measurement Group, MIT, Cambridge, MA 02139-4307, USA

Email Address: mingda@mit.edu

Keywords: *machine learning, equivariant neural networks, Kramers-Krönig relations, photovoltaic materials, quantum materials, optical spectra*

Optical properties in solids, such as refractive index and absorption, hold vast applications ranging from solar panels to sensors, photodetectors, and transparent displays. However, first-principles computation of optical properties from crystal structures is a complex task due to the high convergence criteria and computational cost. Recent progress in machine learning shows promise in predicting material properties, yet predicting optical properties from crystal structures remains challenging due to the lack of efficient atomic embeddings. Here, we introduce GNNOpt, an equivariance graph-neural-network architecture featuring automatic embedding optimization. This enables high-quality optical predictions with a dataset of only 944 materials. GNNOpt predicts all optical properties based on the Kramers-Krönig relations, including absorption coefficient, complex dielectric function, complex refractive index, and reflectance. We apply the trained model to screen photovoltaic materials based on spectroscopic limited maximum efficiency and search for quantum materials based on quantum weight. First-principles calculations validate the efficacy of the GNNOpt model, demonstrating excellent agreement in predicting the optical spectra of unseen materials. The discovery of new quantum materials with high predicted quantum weight, such as SiOs which hosts exotic quasiparticles, demonstrates the potential of GNNOpt in predicting optical properties across a broad range of materials and applications.

1 Introduction

Understanding the optical properties of materials is crucial for designing and optimizing optoelectronic devices such as LEDs, solar cells, photodetectors, and photonic integrated circuits (PICs). These devices play an indispensable role in the current resurgence of the semiconductor industry [1, 2, 3, 4]. The linear optical responses, in particular, offer insights into fundamental parameters such as energy bandgaps, transparency, reflectivity, and refractive index, which are essential for controlling the light-matter interactions [5, 6]. Tremendous scientific and industrial interests have driven both experimental and computational efforts toward high-throughput screening of candidate materials for tailored optical applications. Current experimental techniques, including ellipsometry, UV-Vis spectroscopy, and Fourier transform infrared spectroscopy (FTIS), are commonly used to obtain materials' optical spectra. However, they are limited to specific wavelength ranges and often require stringent sample conditions, making them unideal for high-throughput material screening [7, 8, 9, 10]. On the other hand, first-principles calculations based on density functional theory (DFT) can compute optical spectra across all wavelength ranges [11]. However, DFT requires dense k-point sampling for the convergence of complex dielectric functions or absorption coefficients. For instance, in graphite, the transition of excited electrons by light occurs near the Dirac point, necessitating a k-point sampling of over 100,000 k-points to accurately capture the optical transitions, resulting in a time-consuming calculation [12]. Consequently, high-throughput DFT calculations for optical spectra are largely limited to materials with a small number of atoms per unit cell [13].

Machine-learning methods are increasingly being adopted in materials research to accelerate materials discovery through high-throughput property prediction [14, 15, 16]. One successful approach is the use of graph neural networks (GNNs) to predict material properties directly from crystal structures [17, 18, 19]. Chen *et al.* [19] build a GNN model using an equivariant neural network with E(3)NN [20], which predicts the phonon density-of-states (DOS) by using only atomic species and positions as input parameters. The success of machine learning models in structure-property prediction suggests a potential for applying machine learning to optical spectra prediction. However, challenges remain in developing an effective model that not only accurately predicts optical properties from a small available database, but also extracts useful information from complex relationships in optical spectra, such as the Kramers–Krönig (K-K) relations and the f -sum rule [21]. Such a model could be instrumental in searching for photovoltaic materials for energy conversion or in understanding fundamental physics through the optical spectra of materials.

In this work, we develop GNNOpt, a GNN model that establishes a direct relationship between crystal structures and frequency-dependent optical properties. Rather than focusing on building a more complex neural network structure, we emphasize automatic embedding optimization on top of the equivariant neural networks. This approach surpasses the commonly-used fixed embedding schemes, and goes beyond the feature selection and importance method by integrating different features through additional neural networks. This enables high-quality optical predictions with a small dataset of 944 materials [13, 22]. In a GNN model, converting crystal structure into machine-readable graph representations is essential. While the distance vector between an atom and its neighbor is a mandatory fixed embedding for applying the equivariant neural networks in E(3)NN [20], particularly as input parameters of the spherical harmonics in a tensor product, the feature embedding, or representation of an atom, serve as initial parameters and often relies on human intuition to select the best descriptors in a GNN. For phonon DOS predictions, atomic mass is a natural embedding [19, 23]. However, atomic mass is less relevant for optical properties, and identifying suitable atomic embeddings can be challenging since there are various physical, chemical, structural, and environmental descriptors available. To address this challenge, we propose an ensemble embedding layer for the GNN model. The ensemble embedding layer assigns a learnable weight to each feature embedding. As a result, the GNN model can automatically identify the most important descriptors for specific physical properties from several selected descriptors. Combining the ensemble embedding and the equivariant neural networks, our GNN model can directly and accurately predict optical spectra using only crystal structure as input, which shows superior performance than any fixed embeddings. Additionally, thanks to the K-K relation, we were able to extract all frequency-dependent optical spectra, such as the absorption coefficient, the refractive index, and reflectivity, from only the real (or imaginary) part of the dielectric function. Thus, our predictive model can capture the main features of all-optical spectra, even for crystal structures with unseen elements. By predicting the optical spectra in 5,281 unseen crystal structures, we identify a list of high-performing materials for solar cell application, supported by additional first-principles calculations. The f -sum rule is another universal constraint in the linear optical response, which determines the quantum characteristics of a material by integrating over an infinite spectral range. A recent theory shows that quantum weight, a parameter based on the variation of f -sum rule [24], is directly connected to the ground state quantum geometry and topology. Using quantum weight, our GNNOpt model successfully identifies several quantum materials with high quantum weight, such as SiOs, validated by first-principles calculations. Thus, our work presents an efficient approach to obtaining optical spectra directly from crystal structures, offering diverse applications in materials science.

2 GNNOpt: A machine learning model for optical spectra prediction

The input and output of the GNNOpt are shown in **Figure 1a**, in which the crystal structure is only the input parameter for the GNNOpt and the optical spectra including complex dielectric function ($\epsilon_1(\omega)$ is the real part and $\epsilon_2(\omega)$ is the imaginary part), absorption coefficient ($\alpha(\omega)$), complex refractive index ($n(\omega)$ is the real part and $k(\omega)$ is the imaginary part), and reflectance ($R(\omega)$), where ω is the angular frequency of light and the photon energy is given by $E = \hbar\omega$, where \hbar is the reduced Planck constant. All optical spectra are related together by the Kramers–Krönig relations, which will be discussed in the

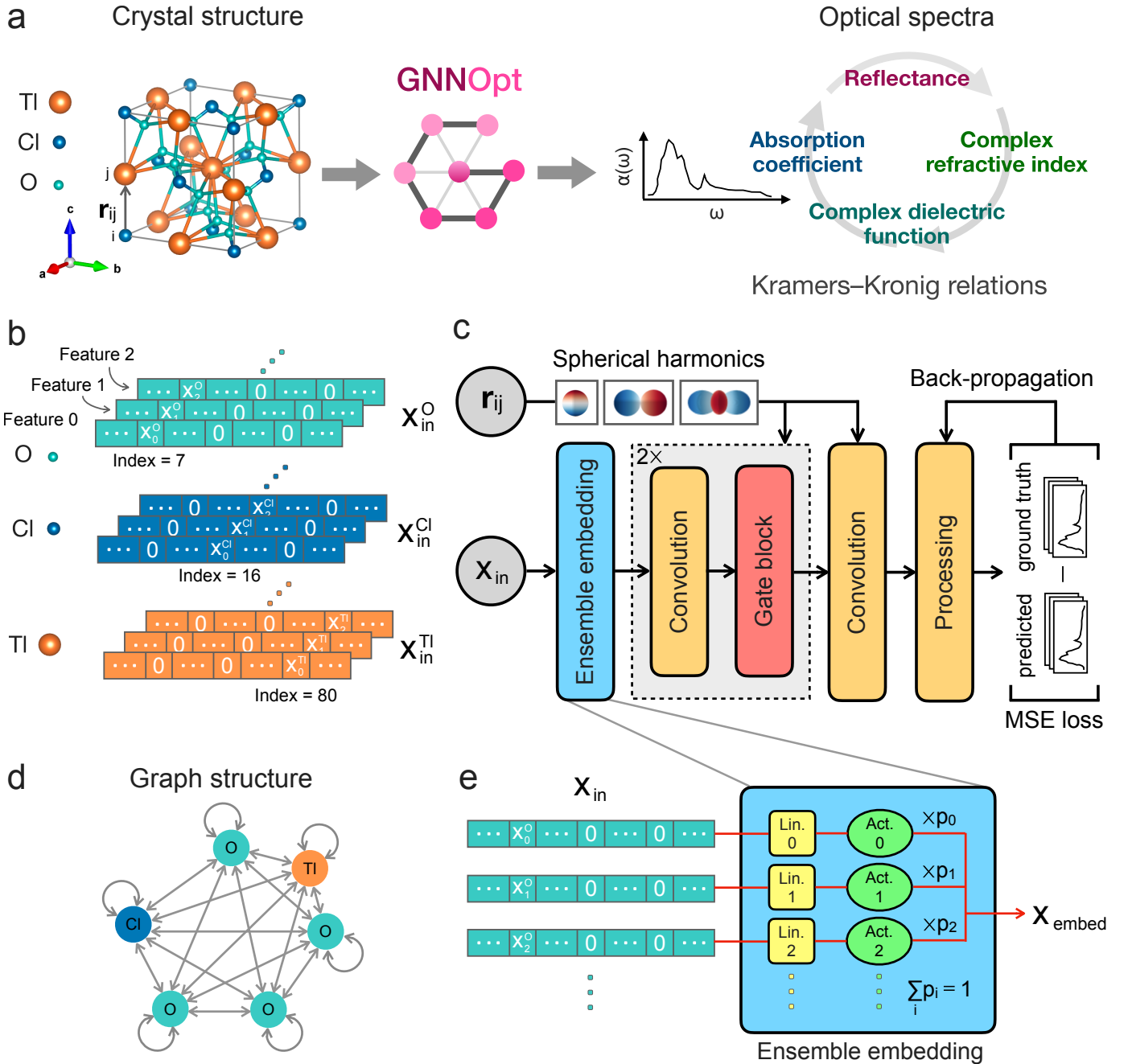


Figure 1: The GNNOpt for optical spectra prediction. **a.** The crystal structure is the only input parameter needed for the GNNOpt to predict the optical spectra, taking TiClO_4 as an example. r_{ij} is a distance vector between i -th and j -th atoms, and a number of frequency-dependent optical properties can be predicted. **b.** Input features of each atomic species (O, Cl, and Ti) in feature-weighted one-hot representation, which is a 118-element-long array of zeroes except an element with an index equal to the atomic number where the value is equal to the feature. **c.** Overview of the GNNOpt architecture. All atomic input features are automatically optimized by an ensemble embedding layer. Then, the embedded features are passed through a sequence of equivariant graph convolution and gated nonlinear layers parameterized with r_{ij} 's radial and spherical harmonic representations. After that, the result is passed to a post-process layer, including activation and aggregation, to generate the predicted output spectra. Finally, the network weights are trained by minimizing the mean-square error (MSE) loss function between the predicted and ground-truth spectra. **d.** Graph representation of periodic lattice of TiClO_4 , where the graph nodes represent the atoms inside a unit cell, and edges represent message passing directions of graph convolutions. **e.** In an ensemble embedding layer, each atomic feature is independently embedded with its linear layer (Lin. 0, Lin. 1, ...) and activation layers (Act. 0, Act. 1, ...). After that, all embedded features are weighted and averaged by learnable weight probability p_i . The same ensemble embedding layer's parameter values are used across all elements, allowing interpretability of the model feature importance.

next paragraph. In **Figure 1b**, we show the input features of each atomic species (or each node), in which we adopt three features, including the atomic mass (x_0), dipole polarizability (x_1), and the effective covalent radius (x_2). All input features use a one-hot encoding to denote the atomic species. For example, the oxygen atom is encoded as $[0, \dots, x_0^O, \dots, 0]$ for the feature 0 (i.e., atomic mass) with a 118-element-long array of zeroes except for an element with an index = 8, which equals to the atomic number of the oxygen minus one. Similarly, we have $[0, \dots, x_1^O, \dots, 0]$ and $[0, \dots, x_2^O, \dots, 0]$ for the feature 1 (dipole polarizability) and the feature 2 (covalent radius), respectively. Thus, the one-hot representation of the oxygen atom with three features is $\mathbf{x}_{\text{in}}^O = ([0, \dots, x_0^O, \dots, 0]; [0, \dots, x_1^O, \dots, 0]; [0, \dots, x_2^O, \dots, 0])$. After that, all input features of each atom are automatically optimized for their embedding mixture by an ensemble embedding layer, as shown in **Figure 1c**. Then, the embedded features are passed through a sequence of equivariant graph convolution and gated nonlinear layers parameterized with the input parameter \mathbf{r}_{ij} . Here, \mathbf{r}_{ij} is a distance vector between i -th atom and neighbor j -th atoms up to a radial cut-off value $r_{\text{cut}} = 6$ Å (see **Figure 1a**). Here, the periodic boundary condition is considered when constructing a graph. To achieve the equivariance, the convolutional filters are designed to be composed of learnable radial functions $R(|\mathbf{r}_{ij}|)$ and spherical harmonics $Y_\ell^m(\mathbf{r}_{ij}/|\mathbf{r}_{ij}|)$, where the indices ℓ and m indicate the degree and order of the function. Therefore, the geometric information and all crystallographic symmetries of input crystal structures are preserved in GNNOpt. After the final convolution layer, all resulting features are summed and passed through a processing layer, including activation (ReLU) and normalization (using the median value of ground truth) steps to predict the optical spectra. The weights of the GNNOpt are optimized by minimizing the mean squared error (MSE) loss function between the predicted and ground truth spectra. Figure 1d shows the graph representation of a unit-cell TiClO_4 , in which nodes represent atoms of a unit cell, and edges represent the message passing direction of graph convolutions layers. In **Figure 1e**, we show the detail of the ensemble embedding layer, which is the key to performance improvement even without any neural network model change. For each atom, each feature is independently embedded with its linear and activation layers. After that, all embedded features are evaluated by a weighted average by learnable mixing probability p_i , in which p_i are normalized by $\sum_i p_i = 1$ (see Method Section for the full hyperparameters of the GNNOpt).

Next, we apply GNNOpt to predict the optical spectra given the limited training data with 944 materials, which are calculated by DFT within the independent-particle approximation (IPA) [13]. The database is obtained from the Material Project [22]. The details for the data preparation and statistics are given in Section 7.1 and **Figure S1** in the Supporting Information. We note that the linear optical properties are not independent but follow the K-K relations [21, 25]:

$$\epsilon_1(\omega) = 1 + \frac{2}{\pi} P \int_0^\infty \frac{\epsilon_2(\omega') \omega'}{\omega'^2 - \omega^2} d(\omega'), \quad (1)$$

$$\epsilon_2(\omega) = -\frac{2\omega}{\pi} P \int_0^\infty \frac{\epsilon_2(\omega') \omega'}{\omega'^2 - \omega^2} d(\omega'), \quad (2)$$

$$\alpha(\omega) = \frac{\sqrt{2}\omega}{c} \sqrt{\sqrt{\epsilon_1^2(\omega) + \epsilon_2^2(\omega)} - \epsilon_1(\omega)}, \quad (3)$$

$$n(\omega) = \sqrt{\frac{1}{2} \left(\sqrt{\epsilon_1^2(\omega) + \epsilon_2^2(\omega)} + \epsilon_1(\omega) \right)}, \quad (4)$$

$$k(\omega) = \sqrt{\frac{1}{2} \left(\sqrt{\epsilon_1^2(\omega) + \epsilon_2^2(\omega)} - \epsilon_1(\omega) \right)}, \quad (5)$$

$$R(\omega) = \frac{(n(\omega) - 1)^2 + k^2(\omega)}{(n(\omega) + 1)^2 + k^2(\omega)}, \quad (6)$$

where P in Equations (1) and (2) denotes the Cauchy principal value. The database, which originally only included ϵ_1 , ϵ_2 , and α , is expanded for n , k , and R by using Equations (4), (5), and (6), respectively. It is noted that only the averaged optical values, i.e., $\alpha = (\alpha_{xx} + \alpha_{yy} + \alpha_{zz})/3$, are available in the database [13].

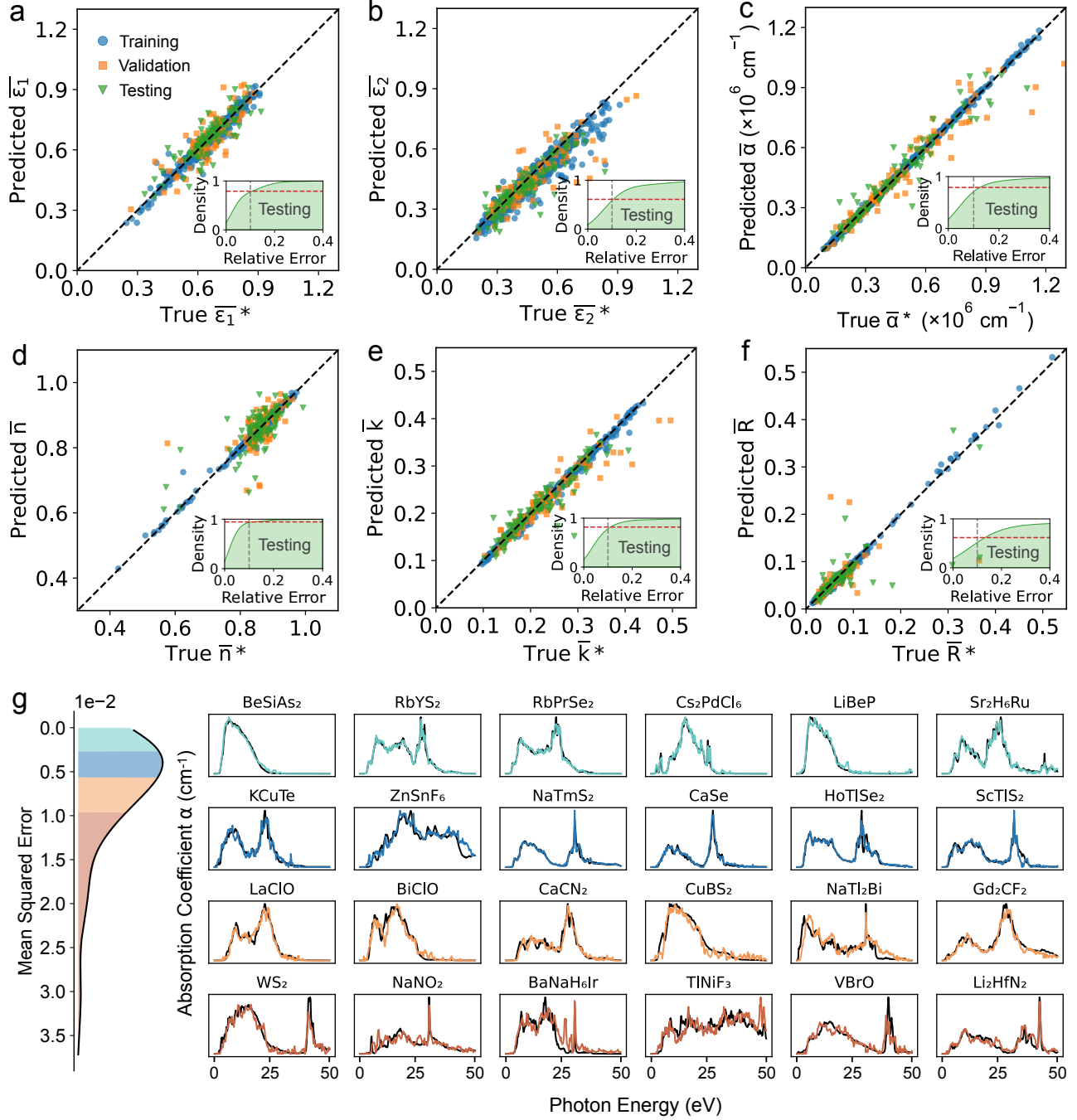


Figure 2: Performance of the GNNOpt in predicting different optical properties. a–f. Weighted average magnitudes of a few optical properties predicted from the GNNOpt model, \bar{W} , compared with the ground-truth (true), \bar{W}^* , with the $\bar{W} = \bar{\epsilon}_1, \bar{\epsilon}_2, \bar{\alpha}, \bar{n}, \bar{k}$, and \bar{R} , for complex dielectric function, absorption coefficient, complex refractive index, and reflectance, respectively. The data points of circle (blue), square (orange), and triangle (green) denote the training, validation, and testing datasets, respectively. The inset shows the cumulative kernel-density-estimator (KDE) plot of the relative error, $|\bar{W} - \bar{W}^*|/\bar{W}^*$, of the only testing dataset. g. Mean squared error (MSE) distribution and 24 randomly selected materials in the test dataset corresponding to each error quartile in the MSE distribution for absorption coefficient $\alpha(\omega)$. Color lines are the GNNOpt-predicted spectra, and black lines are the DFT ground-truth spectra.

Optic	Fixed embedding			Ensemble embedding	
	Atomic mass	Dipole polarizability	Covalent radius	Ensemble	Probability (p_0, p_1, p_2)
ϵ_1	0.69	0.67	0.72	0.72	0.0021, 0.0017, 0.9962
ϵ_2	0.62	0.63	0.58	0.74	0.0026, 0.0002, 0.9972
α	0.93	0.93	0.91	0.93	0.0001, 0.0008, 0.9991
n	0.48	0.51	0.48	0.51	0.0011, 0.0013, 0.9976
k	0.85	0.86	0.85	0.86	0.0001, 0.0002, 0.9997
R	0.61	0.48	0.57	0.55	0.0033, 0.0018, 0.9949

Table 1: The coefficient of determination, R^2 , of the test set with the fixed embedding and ensemble embedding layer. The feature embedding: atomic mass, dipole polarizability, or covalent radius is used in the fixed embedding, while ensemble embedding considers three feature embeddings.

To compare the predicted spectra with the DFT ground-truth spectra, we calculate the weighted mean, \overline{W} , of the optical spectra, $W(\omega)$, by

$$\overline{W} = \frac{\int d\omega W(\omega)\omega}{\int d\omega W(\omega)}, \quad (7)$$

where $W(\omega)$ denotes the optical spectra, such as $\epsilon_1(\omega)$, $\epsilon_2(\omega)$, $\alpha(\omega)$, $n(\omega)$, $k(\omega)$, or $R(\omega)$. The corrections between the GNNOpt-predicted, \overline{W} , and DFT ground-truth spectra, \overline{W}^* are plotted in **Figure 2a–f**. Here, the coefficients of determination, R^2 , of the test set are 0.72, 0.74, 0.93, 0.51, 0.86, and 0.55 for ϵ_1 , ϵ_2 , α , n , k , and R , respectively, which show excellent agreement for the cases of α and k . On the other hand, the relative error $|\overline{W} - \overline{W}^*|/\overline{W}^*$ below 10% for the test set (see the inset figures) of ϵ_1 , ϵ_2 , α , n , k , and R are 79%, 61%, 79%, 95%, 82%, and 62%, respectively, which shows the high performance of our model to predict ϵ_1 , α , n , and k . To visualize the model performance, in **Figure 2g**, we also plot $\alpha(\omega)$ of the 24 randomly selected materials from the test set in each mean-squared-error (MSE) quartile, in which the color lines are the GNNOpt-predicted spectra and the black lines are the DFT ground-truth spectra. In **Figure 2g**, the 1st to 4th rows in the right figure correspond to the 1st to 4th error quartiles in the left figure by the same color. The overlap between the predicted $\alpha(\omega)$ (color lines) and the DFT calculation (black line) in **Figure 2g** suggests that our model can accurately predict optical spectra, in which all spectrum peaks are reproduced from the DFT calculation even for the 4th row. In the 3rd and 4th rows, some noise can be found in the predicted $\alpha(\omega)$ of NaTi₂Bi or TiNiF₃. This is because of the origin of the Dirac delta function in the dielectric function formula, which is often solved by adopting a broadening parameter or increasing the number of k-point samples in the DFT calculation [11]. For the GNNOpt model, a uniform filter of the SciPy library [26] can be applied instead of the broadening parameter in the DFT to reduce the noise of the spectrum. The MSE loss and the compared full spectra of the training, validation, and testing datasets for ϵ_1 , ϵ_2 , α , n , k , and R are given in **Figures S4–S10** in the Supporting Information, respectively.

In **Table 1**, we compare the R^2 values of the test set with the ensemble embedding layer and fixed embeddings. In this present study, we use three feature embeddings: atomic mass, dipole polarizability, and covalent radius, since these features are provided for all elements in the periodic table. Nevertheless, the ensemble embedding layer can work with any other added features. Table 1 shows the performance improvement of the GNNOpt with the ensemble embedding layer for ϵ_2 . For other optical spectra, the GNNOpt with the ensemble embedding layer is comparable with the best-trained fixed embedding model. On the other hand, the value of p_i of the ensemble embedding layer can tell us which feature is the main contribution. For the GNNOpt, the mixing probability shows that the covalent radius (feature 2) is almost completely dominant with $p_2 \approx 1$. We note that the covalent radius is a measure of the size of an atom that forms part of one covalent bond [27]. On the other hand, the dipole moment, which is related to the optical properties, is defined as the product of the total amount of charge and the covalent bond length. This relationship might explain why the covalent radius is the most dominant feature in the GNNOpt.

To evaluate the scalability of the GNNOpt model for unseen materials, we perform the GNNOpt with the test set containing larger atomic site numbers N_{test} than the training and validation sets. There are

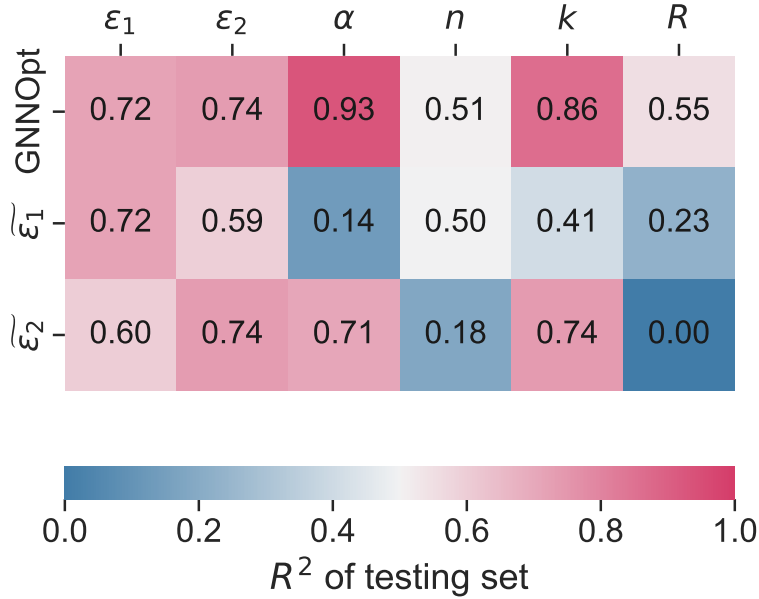


Figure 3: Coefficient of determination R^2 of the test set for the optical spectra $W = \epsilon_1, \epsilon_2, \alpha, n, k$, and R . For the 1st row, W is directly predicted by using GNNOpt. For the 2nd and 3rd rows, W is calculated from the predicted $\tilde{\epsilon}_1$ and $\tilde{\epsilon}_2$ by using the Kramers-Krönig relations, respectively.

there cases of the test set as $N_{\text{test}} = 8, 9$ (case I), $N_{\text{test}} = 7, 8, 9$ (case II), and $N_{\text{test}} = 6, 7, 8, 9$ (case III). As shown in **Figures S11a-c**, R^2 for the test set are 0.83, 0.84, and 0.86 for the cases I, II, and III, respectively. Moreover, the training set contains only 443 materials with $2 \leq N_{\text{train}} \leq 5$ in case III. However, the prediction optical spectra show a good overlap with the DFT ground truth for the test set with $6 \leq N_{\text{test}} \leq 9$ (see Figure S11d). Thus, it suggests that the GNNOpt can accurately predict the optical properties of unseen complex materials with larger systems than the training set.

3 The Kramers-Krönig relations

To evaluate the Kramers-Kronig relations for predicted optical properties, first, we use the complex dielectric function $\tilde{\epsilon}_1$ and $\tilde{\epsilon}_2$, which are predicted by the GNNOpt, to calculate other optical properties by using Equations (1)-(6). Then, we calculate the R^2 coefficients for the test set for each of the optical properties. Finally, we compare these R^2 values from the K-K relations with R^2 of the corresponding optical properties from GNNOpt, as shown in **Figure 3**. It notes that we use the same training, validation, and test sets for all cases. The highest R^2 value in the 1st row suggests that directly predicting the optical properties is better than calculating the optical properties from the predicted $\tilde{\epsilon}_1$ (or $\tilde{\epsilon}_2$). In other words, the K-K relations must be applied before the GNNOpt model to predict optical spectra, i.e., $\epsilon_1(\epsilon_2) \rightarrow$ K-K relations $\rightarrow W \rightarrow$ GNNOpt \rightarrow predicted- W . In the 2nd and 3rd rows of Figure 3, R^2 of $\alpha/\tilde{\epsilon}_2$ (0.71) and $k/\tilde{\epsilon}_2$ (0.74) are larger than that of $\alpha/\tilde{\epsilon}_1$ (0.14) and $k/\tilde{\epsilon}_1$ (0.41). This implies that α and k are more dependent on ϵ_2 than ϵ_1 , which is clearly explained by Equations (3) and (4), $\alpha(\omega) = 2\omega k(\omega)/c \propto \sqrt{|\epsilon_2|}$. In contrast, R^2 of $n/\tilde{\epsilon}_1$ (0.50) and $R/\tilde{\epsilon}_1$ (0.23) are larger than that of $n/\tilde{\epsilon}_2$ (0.18) and $R/\tilde{\epsilon}_2$ (0.00). That means that n and R are more dependent on ϵ_1 than ϵ_2 . R^2 of $\epsilon_1/\tilde{\epsilon}_1$ (0.72) and $\epsilon_2/\tilde{\epsilon}_2$ (0.74) are same with that of GNNOpt since $\epsilon_1 = \tilde{\epsilon}_1$ and $\epsilon_2 = \tilde{\epsilon}_2$. By evaluating the K-K relations before and after training the GNNOpt model, we found that the K-K relations should be applied before training the model.

4 Screening solar cell materials

The first application of the GNNOpt is to identify potential solar cell materials with high-performance energy conversion. For this task, Shockley-Queisser (SQ) limit is a key factor to estimate the upper limit for solar-energy conversion efficiency [28]. However, the SQ limit assumes that the absorption coefficient is a step function or the infinity thickness of the absorber material. An alternative parameter that is more suitable for real PV materials and devices is introduced by Yu and Zunger [29], which is the spectroscopic limited maximum efficiency (SLME). For the SLME method, the efficiency of the energy conversion, η , is defined as the ratio between the maximum output power density, P_{out} , and the incident solar power density, P_{solar} ,

$$\eta = \frac{P_{\text{max}}}{P_{\text{solar}}}. \quad (8)$$

P_{max} and P_{solar} can be written in terms of $J - V$ characteristic of the solar cell and the solar spectrum, respectively [29]:

$$P_{\text{max}} = \max\{JV\}_V = \max\{[J_{\text{sc}} - J_0(e^{qV/k_B T} - 1)]V\}_V, \quad (9)$$

and

$$P_{\text{solar}} = \int_0^\infty EI_{\text{solar}}(E)dE, \quad (10)$$

respectively, where J is the total current density, V is potential over the absorber layer, k_B is the Boltzmann constant, T is the temperature of the solar device, q is the elementary charge. J_{sc} and J_0 are the short-circuit current density and the reverse saturation current density, respectively, which depend on the absorption coefficient, $\alpha(E)$, and the thickness, L , of the material as follows [29]:

$$J_{\text{sc}} = q \int_0^\infty [1 - e^{-2\alpha(E)L}] I_{\text{solar}}(E)dE \quad (11)$$

and

$$J_0 = \frac{J_0^r}{f_r} = \frac{q\pi}{f_r} \int_0^\infty [1 - e^{-2\alpha(E)L}] I_{\text{bb}}(E, T)dE, \quad (12)$$

where $I_{\text{solar}}(E)$ is the AM1.5G solar spectrum, $I_{\text{bb}}(E, T)$ is the black-body spectrum, and f_r is the radiative recombination current density. From Equations (8)-(12), the material property-related inputs $\alpha(E)$, L , T , and f_r are required to calculate the SLME. In this work, we assume the $L = 500$ nm, $T = 300$ K, and the radiative recombination is the only recombination process, i.e., $f_r = 1$, which is a good approximation for the materials where radiative recombination dominates, such as GaAs [30]. Since the solar spectrum for solar energy harvesting ranges from 200 – 2500 nm (i.e., 0.5 – 6.0 eV), we thus retrain the GNNOpt model with the photon energy < 10 eV, which is sufficient for the SLME calculation.

In **Figure 4a**, we compare the predicted and true efficiencies for the test set, in which $R^2 = 0.81$ shows a high prediction accuracy of the GNNOpt for the SLME. Using the trained GNNOpt model, we predict the η values of 5,281 unseen crystal structures from the Materials Project without ground-truth optical spectra [22]. Here, we select only the stable insulators with an energy band gap E_g , suitable for solar-energy harvesting applications ($0 \leq E_g \leq 5.0$ eV). Statistical plots of the unseen materials with the number of materials as a function of E_g , N , and lattice constant are shown in **Figure S12** in Supplementary Information. In **Figure 4b**, we plot the predicted- η as a function of E_g . We observe that the maximum η is about 32% at $E_g \sim 1.3$ eV, which is consistent with the SQ limit. However, the SLME is a more stringent selection parameter than the SQ limit for the solar cell materials because the SLME shows η values over a wide range for materials with similar band gaps, indicating the significant contribution of $\alpha(E)$ to η .

Additionally, knowing which elements from the periodic table contribute most to high-efficiency solar cell materials can serve as an initial guideline for material design. As presented in **Figure 4c**, the transition metals such as Tc, Rh, Pd, Pt, Cu, Ag, Au, and Hg, and chalcogenides including S, Se, and Te, are the main constituent elements of the solar cell materials. This finding is in agreement with widely known solar cell materials, such as Cu-rich chalcopyrite [31], Pb-based perovskites [32, 33], or CdTe [34]. In **Table S1**

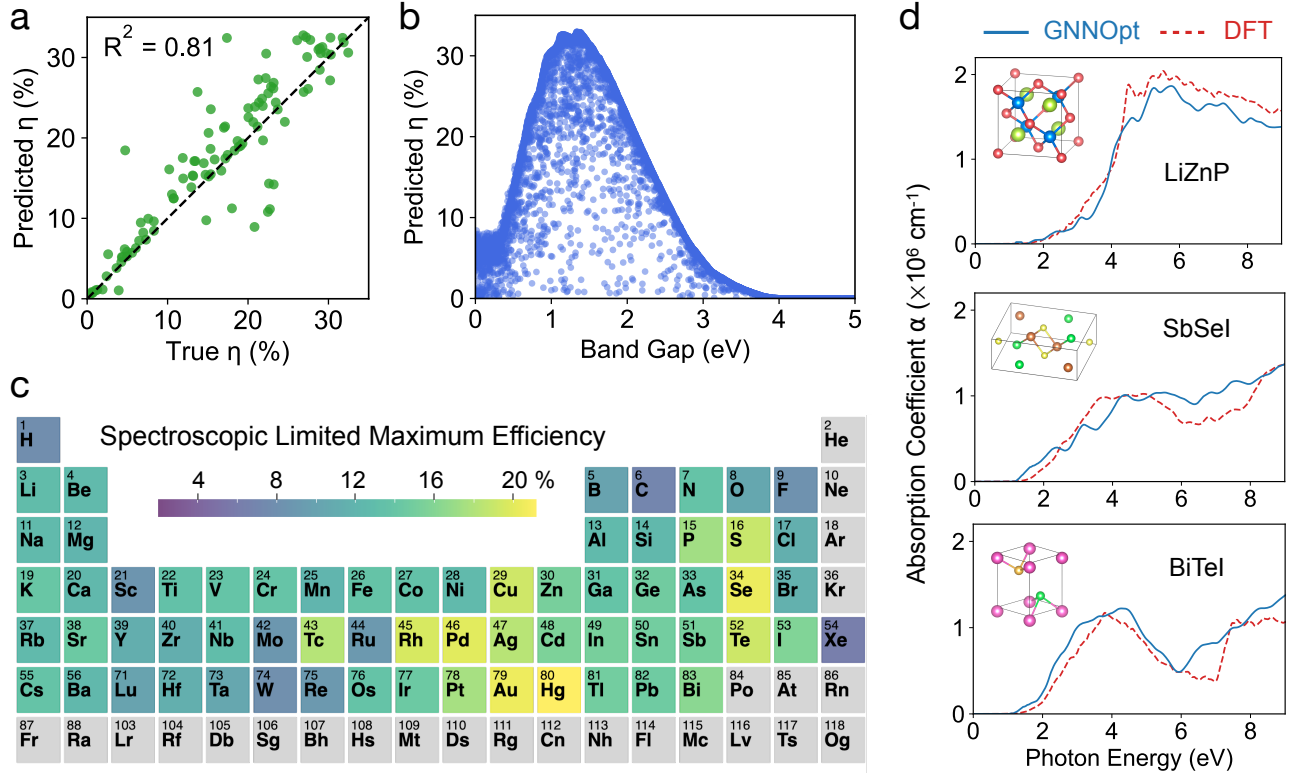


Figure 4: Searching material candidates for solar energy harvesting applications with GNNOpt. **a.** Comparison between predicted and true efficiencies η , obtained by the GNNOpt and the DFT ground truth, respectively, for the test set. Here, η is estimated by the spectroscopic limited maximum efficiency (SLME). **b.** η -predicted by the GNNOpt of the 5,281 stable materials from the Material Project, which is plotted as a function of the energy band gap. **c.** The periodic table is colored by the SLME of materials containing each element. **d.** Absorption coefficients $\alpha(E)$ are plotted as a function of photon energy E by using the GNNOpt (solid lines) and the DFT (dashed lines) for the unseen materials, including LiZnP, SbSeI, and BiTeI. The inset figures show the crystal structures of these materials.

in Supplementary Information, we identified 246 materials with η -SLME greater than 32%. To validate the predicted SLME of the unseen materials, we selected three examples from the highest-SLME materials list: LiZnP, SbSeI, and BiTeI. These materials are not present in the DFT database. We conducted DFT calculations to determine $\alpha(E)$ in these examples. The results, depicted in **Figure 4d**, show excellent agreement between the DFT calculations (dashed lines) and the GNNOpt-predicted α values (solid lines). This indicates that GNNOpt could be an effective materials screening tool at a much lower computational cost.

5 Probing quantum materials

In this section, we provide another application scope of GNNOpt to probe quantum geometry and topology in quantum materials. Since the dipole moment matrix element for optical transition is closely related to the interband Berry connection [35], recent studies have established the relationship between the quantum geometry and the optical properties [36, 37, 38]. In particular, very recently, Onishi and Fu [24] theoretically showed that the generalized quantum weight, a concept that can be derived from optical spectra, is a direct measure of ground state quantum geometry and topology. The quantum weight K_{xx} is given by a modification of f -sum rule weighted by the inverse frequency as follows [24]:

$$K_{xx} = \frac{2\hbar}{e^2} \int_0^\infty \frac{\text{Re}[\sigma_{xx}(\omega)]}{\omega} d\omega = \frac{2\hbar}{e^2} \int_0^\infty \epsilon_2(\omega) d\omega, \quad (13)$$

where $\text{Re}[\sigma_{xx}(\omega)]$ is the real part of optical conductivity over the entire frequency range (i.e., $0 < \omega < \infty$).

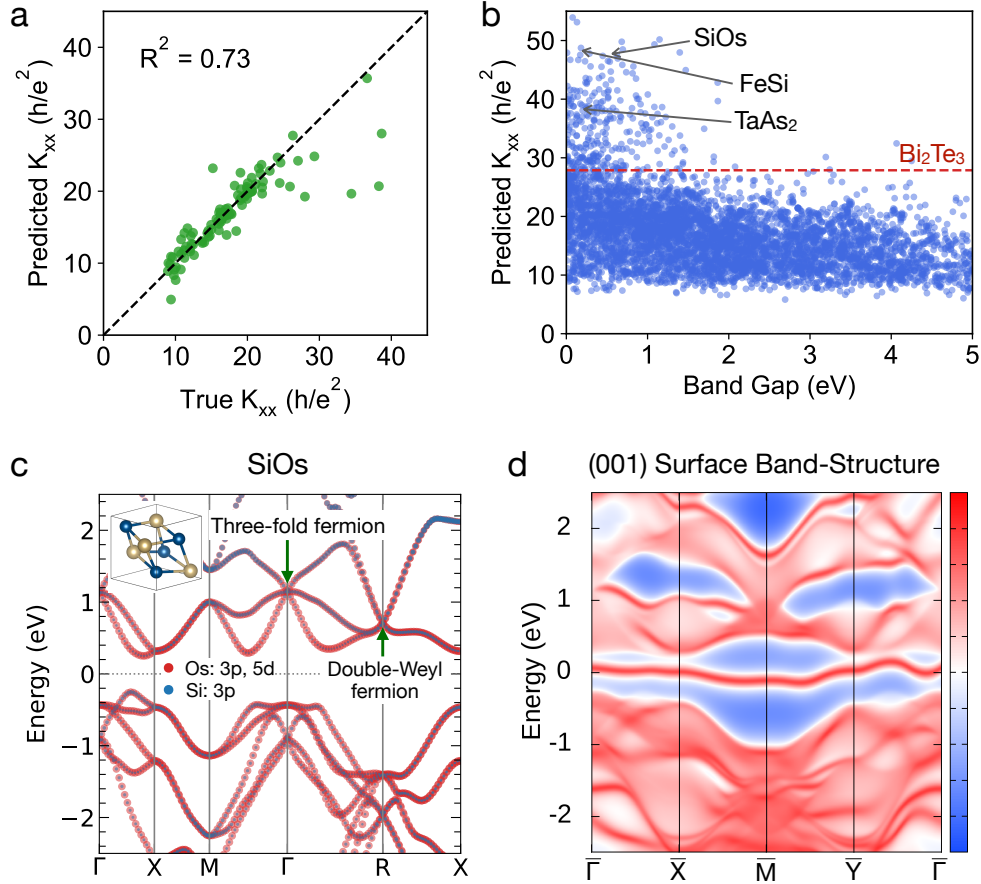


Figure 5: Searching for quantum materials with high Quantum weight K_{xx} using GNNOpt. **a.** Comparison between predicted and true K_{xx} , obtained by the GNNOpt and the DFT ground truth, respectively, for the test set. **b.** K_{xx} -predicted by the GNNOpt of the 5,281 stable materials from the Material Project, which is plotted as a function of the energy band gap. The dashed line indicates $K_{xx} = 27.87$ of Bi_2Te_3 . **c.** Electronic band structure with atomic orbital projections in the color of the high- K_{xx} material, SiOs. The arrows indicate the double-Weyl and three-fold fermions at the Γ and R points, respectively. **d.** The surface band structure along the high-symmetry lines on the (001) surface of SiOs. The color bar scale is in arbitrary units.

The GNNOpt for prediction $\epsilon_2(\omega)$ with $0 < \omega < 50$ eV (see **Figure S6**) is used to obtain K_{xx} . It is noted that for $\omega > 50$ eV, $\epsilon_2(\omega) \rightarrow 0$ for all materials in the training set. In **Figure 5a**, we compare the predicted and true K_{xx} in the unit of h/e^2 for the test set. $R^2 = 0.73$ shows a good prediction between the GNNOpt and the DFT, particularly for $K_{xx} < 25$. The GNNOpt is thus used to predict K_{xx} of the 5,281 unseen insulator materials, as shown in **Figure 5b**. For simplicity, we consider the quantum weight of the well-known topology insulator Bi_2Te_3 ($K_{xx} = 28.87$) as a threshold for classifying quantum materials, in which the material with $K_{xx} > 28.87$ is considered as the high- K_{xx} materials. We identified 297 high- K_{xx} materials, listed in **Table S2** in Supplementary Information, in which several materials, such as ZrTe_5 ($K_{xx} = 33.90$), TaAs_2 ($K_{xx} = 37.66$), FeSi ($K_{xx} = 48.74$), and NbP ($K_{xx} = 35.58$), etc., have been reported as quantum materials with anomalous hall effect [39], large magnetoresistance [40], topological Fermi arcs [41], and quantum oscillations [42].

To further validate the quantum characteristics from the predicted high- K_{xx} materials, we carry out additional DFT calculations for SiOs, which have exceedingly high quantum weight ($K_{xx} = 46.52$) but have not been well studied. As shown in **Figure 5c**, SiOs is found to host the three-fold and double-Weyl fermions at the Γ and R points, respectively. Since both the three-fold and double-Weyl fermions are located above the Fermi level (at 1.15 eV and 0.7 eV, respectively), it would not be possible to detect them using the angular resolved photoemission spectroscopy (ARPES) technique. Nevertheless, irrespective of the energy position of the manyfold band crossing points, we could expect the associated Fermi surface arcs on the surface Brillouin zone [43, 44]. We thus calculated the surface band structure of the (001) SiOs

by using the maximally-localized Wannier functions and the Green’s function approach (see Method). As shown in **Figure 5d**, we find the surface state near the Fermi level form self-enclosed loops, indicating the triviality of these states, in contrast to the open Fermi arcs. This closed-loop shrinks in size when the surface state moves away from the Fermi energy (see **Figure S15a**). However, the nontrivial topological Fermi arcs associated with manifold fermions can be found at 1.3 eV above the Fermi level (see Figure S15b). These signatures suggest the ultra-quantum properties of SiOs.

6 Discussions

In this work, we present GNNOpt, a graph neural network model with engineered input embedding that directly predicts all linear optical spectra from crystal structures. The ensemble embedding layer for automatic embedding optimization improves prediction accuracy without modifying the neural network structures. By integrating with the equivariant neural network, GNNOpt achieves high-quality predictions with high data efficiency using a small training set of 944 materials. Furthermore, applying the Kramers-Krönig relation before training the GNNOpt model results in better-predicted optical spectra, as observed by comparing optical properties before and after training. With GNNOpt, we were able to identify over 200 materials with over 32% conversion efficiency for solar energy harvesting applications. Additionally, thanks to the recent connection between optical property and ground-state topology, we were able to screen quantum materials carrying multiple nontrivial topology, including SiOs.

The direct ensemble structure input in GNNOpt opens several promising future research directions. First, the atomic embedding with multiple features greatly facilitates the encoding of defect structures, which could be encoded by perturbing one or more atomic features. Given the significant impact of defects on optical properties, predicting optical properties with defects is highly desirable. This approach could enable tuning absorption spectra through new defect levels or identifying non-radiative recombination centers that reduce solar cell efficiency. Second, building on the successful prediction of linear optical properties, extending this method to second and third-order optical responses, such as second harmonic generation and Raman spectroscopy, offers valuable opportunities. Third, since the current ground truth database is DFT-based, future studies incorporating many-body effects, such as the GW approximation, could provide more accurate predictions, particularly for excitons. Lastly, since the ensemble embedding integrates multiple embedding types to enhance overall model performance and goes beyond feature selection, it is expected to be broadly applicable to other GNN models.

7 Method

7.1 Data preparation for optical spectra

We trained and tested the GNNOptic with the 944 crystalline solids calculated from the density functional theory (DFT) by Yang et al. [13]. The databases are obtained from Materials Project [22] using the API. The optical spectra in the database include the frequency-dependent dielectric function and the corresponding absorption coefficient, which was performed within the independent-particle approximation (IPA). Yang et al. [13] showed that the IPA is sufficient in most cases to reproduce the experiment spectra. The 940 materials in the database were selected based on the energy band gap between $0 \leq E_g \leq 5.0$ eV and the atomic site number $N < 10$ in each unit cell. The static plot of the number of materials as a function of E_g , N , and lattice constants are given in Figure S1 in Supplementary Information.

We randomly split the entire dataset into 80%, 10%, and 10% for the training (733 materials), validation (97 materials), and test (110 materials) sets, respectively (see Figure S2 in Supplementary Information). Given limited training data, the high photon energy ω resolution (with 2001 points) requests a large number of parameters, such as radius cut-off and the number of layers, in the neural network to fit the output dimension. Therefore, to ensure a balanced output dimension and the calculation cost, we interpolate the smoothed spectrum in the range $0 \leq \hbar\omega \leq 50$ eV to 251 points, which is suitable to reproduce all of the spectra peaks (see Figure S3 in Supplementary Information). We also apply the predictive model on 5,281

stable insulators from the Materials Project [22] with $0 \leq E_g \leq 5.0$ eV with atomic site number $N < 20$ in each unit cell. The static plot of the number of materials as a function of E_g , N , and lattice constants for this database are given in Figure S12 in Supplementary Information.

7.2 Hyperparameters optimization

The set of optimized parameters to get the best results for GNNOpt is given as follows: the maximum cutoff radius $r_{\text{cut}} = 6 \text{ \AA}$ the maximum of spherical harmonics $l_{\text{max}} = 2$, the length of the embedding feature vector is 64, the multiplicity of irreducible representation is 32, the number of pointwise convolution layer $n_{\text{conv}} = 2$, the AdamW optimizer learning rate is $(5 \times 10^{-3}) \times 0.96^k$ with k being the epoch number, and the AdamW optimizer weight decay coefficient is 0.05.

7.3 First-principles calculations

We use the Quantum ESPRESSO package for the DFT calculations to obtain the absorption coefficient $\alpha(E)$ of LiZnP, SbSeI, and BiTeI within independent particle approximation [45, 11]. The crystal structures of these materials are taken from the Material Project to be consistent with that in the GNNOpt prediction. The optimized norm-conserving Vanderbilt pseudopotentials [46] with the Perdew–Burke–Ernzerhof exchange–correlation functional [47] are selected for all atoms. A cutoff energy of 60 Ry for plane wave is used for all materials. For self-consistent field (SCF) calculations, the k-points meshes are $6 \times 6 \times 6$, $4 \times 8 \times 3$, and $9 \times 9 \times 5$ for LiZnP, SbSeI, and BiTeI, respectively, while the dense meshes of $20 \times 20 \times 20$, $14 \times 30 \times 12$, and $27 \times 27 \times 15$, respectively, are used for non-SCF calculations in order to achieve convergence in $\alpha(E)$.

To calculate the electronic band structure of SiOs, the tight-binding model is obtained by the maximally-localised Wannier functions using the Wannier90 code [48], in which Si $3p$ and Os $3p, 5d$ orbitals are selected as the basis. Then, the WannierTools code [49] with the Green function approach is used for the analysis of the surface band structure.

Supporting Information

Supporting Information is available from the Wiley Online Library.

Acknowledgements

N.T.H. acknowledges the Researcher, Young Leaders Overseas Program and financial support from the Frontier Research Institute for Interdisciplinary Sciences from Tohoku University. R.O. acknowledges the support from the U.S. Department of Energy (DOE), Office of Science (SC), Basic Energy Sciences (BES), Award No. DE-SC0021940. A.C. thanks National Science Foundation (NSF) Designing Materials to Revolutionize and Engineer our Future (DMREF) Program with Award No. DMR-2118448. M.L. is partially supported by NSF ITE-2345084, the Class of 1947 Career Development Chair and the support from R. Wachnik.

Conflict of Interest

The authors declare no conflict of interest.

Data Availability Statement

The data that support the findings of this study are openly available on GitHub at <https://github.com/nguyen-group/GNNOpt>.

References

- [1] D. Marpaung, J. Yao, J. Capmany, *Nat. Photonics* **2019**, *13*, 2 80.
- [2] W. Bogaerts, D. Pérez, J. Capmany, D. A. Miller, J. Poon, D. Englund, F. Morichetti, A. Melloni, *Nature* **2020**, *586*, 7828 207.
- [3] Y. Meng, Y. Chen, L. Lu, Y. Ding, A. Cusano, J. A. Fan, Q. Hu, K. Wang, Z. Xie, Z. Liu, et al., *Light Sci. Appl.* **2021**, *10*, 1 1.

- [4] F. Priolo, T. Gregorkiewicz, M. Galli, T. F. Krauss, *Nat. Nanotechnol.* **2014**, *9*, 1 19.
- [5] H.-L. Liu, B. D. Annawati, N. T. Hung, D. P. Gulo, P. Solís-Fernández, K. Kawahara, H. Ago, R. Saito, *Phys. Rev. B* **2023**, *107*, 16 165421.
- [6] J. B. Khurgin, *ACS Photonics* **2022**, *9*, 3 743.
- [7] D. P. Gulo, N. T. Hung, R. Sankar, R. Saito, H.-L. Liu, *Phys. Rev. Mater.* **2023**, *7* 044001.
- [8] R. Saito, N. T. Hung, T. Yang, J. Huang, H.-L. Liu, D. P. Gulo, S. Han, L. Tong, *Small* **2024**, 2308558.
- [9] B. C. Smith, *Fundamentals of Fourier transform infrared spectroscopy, 2nd Edition*, CRC Press, Boca Raton, **2011**.
- [10] H.-H. Perkampus, *UV-VIS Spectroscopy and its Applications*, Springer Berlin, Heidelberg, **1992**.
- [11] N. T. Hung, A. R. T. Nugraha, R. Saito, *Quantum ESPRESSO course for solid-state physics*, Jenny Stanford Publishing, Singapore, **2022**.
- [12] D. P. Gulo, N. T. Hung, T.-J. Yang, G.-J. Shu, R. Saito, H.-L. Liu, *Carbon* **2022**, *197* 485.
- [13] R. X. Yang, M. K. Horton, J. Munro, K. A. Persson, *arXiv preprint arXiv:2209.02918* **2022**.
- [14] Y. Liu, T. Zhao, W. Ju, S. Shi, *J. Materiomics*. **2017**, *3*, 3 159.
- [15] G. Genty, L. Salmela, J. M. Dudley, D. Brunner, A. Kokhanovskiy, S. Kobtsev, S. K. Turitsyn, *Nat. Photonics* **2021**, *15*, 2 91.
- [16] R. Pollice, G. dos Passos Gomes, M. Aldeghi, R. J. Hickman, M. Krenn, C. Lavigne, M. Lindner-D'Addario, A. Nigam, C. T. Ser, Z. Yao, et al., *Acc. Chem. Res.* **2021**, *54*, 4 849.
- [17] T. Xie, J. C. Grossman, *Phys. Rev. Lett.* **2018**, *120*, 14 145301.
- [18] F. Scarselli, M. Gori, A. C. Tsoi, M. Hagenbuchner, G. Monfardini, *IEEE Trans. Neural Netw. Learn. Syst.* **2008**, *20*, 1 61.
- [19] Z. Chen, N. Andrejevic, T. Smidt, Z. Ding, Q. Xu, Y.-T. Chi, Q. T. Nguyen, A. Alatas, J. Kong, M. Li, *Adv. Sci.* **2021**, *8*, 12 2004214.
- [20] M. Geiger, T. Smidt, *arXiv preprint arXiv:2207.09453* **2022**.
- [21] V. Lucarini, J. J. Saarinen, K.-E. Peiponen, E. M. Vartiainen, *Kramers-Kronig relations in optical materials research*, volume 110, Springer Berlin, Heidelberg, **2005**.
- [22] A. Jain, S. P. Ong, G. Hautier, W. Chen, W. D. Richards, S. Dacek, S. Cholia, D. Gunter, D. Skinner, G. Ceder, et al., *APL Mater.* **2013**, *1*, 1.
- [23] R. Okabe, A. Chotrattanapituk, A. Boonkird, N. Andrejevic, X. Fu, T. S. Jaakkola, Q. Song, T. Nguyen, N. Drucker, S. Mu, et al., *arXiv preprint arXiv:2301.02197* **2023**.
- [24] Y. Onishi, L. Fu, *Phys. Rev. X* **2024**, *14*, 1 011052.
- [25] D. C. Hutchings, M. Sheik-Bahae, D. J. Hagan, E. W. Van Stryland, *Opt. Quantum Electron.* **1992**, *24* 1.
- [26] P. Virtanen, R. Gommers, T. E. Oliphant, M. Haberland, T. Reddy, D. Cournapeau, E. Burovski, P. Peterson, W. Weckesser, J. Bright, et al., *Nat. Methods* **2020**, *17*, 3 261.
- [27] P. Pyykkö, M. Atsumi, *Chem. - Eur. J.* **2009**, *15* 186.
- [28] W. Shockley, H. J. Queisser, *J. Appl. Phys.* **1961**, *32*, 3 510.

- [29] L. Yu, A. Zunger, *Phys. Rev. Lett.* **2012**, *108*, 6 068701.
- [30] I. Schnitzer, E. Yablonovitch, C. Caneau, A. Ersen, T. Gmitter, In *LEOS'92 Conference Proceedings*. IEEE, **1992** 127–128.
- [31] J. Jiang, R. Giridharagopal, E. Jedlicka, K. Sun, S. Yu, S. Wu, Y. Gong, W. Yan, D. S. Ginger, M. A. Green, et al., *Nano Energy* **2020**, *69* 104438.
- [32] Q. Tai, K.-C. Tang, F. Yan, *Energy Environ. Sci.* **2019**, *12* 2375.
- [33] W. Ke, C. C. Stoumpos, M. G. Kanatzidis, *Adv. Mater.* **2019**, *31* 1803230.
- [34] C. S. Ferekides, D. Marinskiy, V. Viswanathan, B. Tetali, V. Palekis, P. Selvaraj, D. Morel, *Thin Solid Films* **2000**, *361* 520.
- [35] C. Aversa, J. E. Sipe, *Phys. Rev. B* **1995**, *52*, 20 14636.
- [36] J. Ahn, G.-Y. Guo, N. Nagaosa, *Phys. Rev. X* **2020**, *10*, 4 041041.
- [37] T. Holder, D. Kaplan, B. Yan, *Phys. Rev. Res.* **2020**, *2*, 3 033100.
- [38] P. Bhalla, K. Das, D. Culcer, A. Agarwal, *Phys. Rev. Lett.* **2022**, *129*, 22 227401.
- [39] T. Liang, J. Lin, Q. Gibson, S. Kushwaha, M. Liu, W. Wang, H. Xiong, J. A. Sobota, M. Hashimoto, P. S. Kirchmann, et al., *Nat. Phys.* **2018**, *14* 451.
- [40] Y.-Y. Wang, Q.-H. Yu, P.-J. Guo, K. Liu, T.-L. Xia, *Phys. Rev. B* **2016**, *94* 041103.
- [41] S. Changdar, S. Aswartham, A. Bose, Y. Kushnirenko, G. Shipunov, N. Plumb, M. Shi, A. Narayan, B. Büchner, S. Thirupathaiah, *Phys Rev B* **2020**, *101* 235105.
- [42] J. Klotz, S.-C. Wu, C. Shekhar, Y. Sun, M. Schmidt, M. Nicklas, M. Baenitz, M. Uhlarz, J. Wosnitza, C. Felser, et al., *Phys. Rev. B* **2016**, *93* 121105.
- [43] B. Bradlyn, J. Cano, Z. Wang, M. Vergniory, C. Felser, R. J. Cava, B. A. Bernevig, *Science* **2016**, *353* aaf5037.
- [44] Y. Sun, S.-C. Wu, M. N. Ali, C. Felser, B. Yan, *Phys. Rev. B* **2015**, *92*, 16 161107.
- [45] P. Giannozzi, S. Baroni, N. Bonini, M. Calandra, R. Car, C. Cavazzoni, D. Ceresoli, G. L. Chiarotti, M. Cococcioni, I. Dabo, et al., *J. Phys. Condens. Matter* **2009**, *21*, 39 395502.
- [46] D. Hamann, *Phys. Rev. B* **2013**, *88* 085117.
- [47] J. P. Perdew, K. Burke, M. Ernzerhof, *Phys. Rev. Lett.* **1996**, *77* 3865.
- [48] A. A. Mostofi, J. R. Yates, Y. S. Lee, I. Souza, D. Vanderbilt, N. Marzari, *Comp. Phys. Comm.* **2008**, *178*, 9 685.
- [49] Q. Wu, S. Zhang, H.-F. Song, M. Troyer, A. A. Soluyanov, *Comput. Phys. Commun.* **2018**, *224* 405.

Ensemble-Embedding Graph Neural Network for Direct Prediction of Optical Spectra from Crystal Structure: Supplementary Information

Nguyen Tuan Hung,^{*,†} Ryotaro Okabe,[‡] Abhijatmedhi Chotrattanapituk,[‡] and
Mingda Li^{*,‡}

[†]*Frontier Research Institute for Interdisciplinary Sciences, Tohoku University, Sendai
980-8578, Japan*

[‡]*Quantum Measurement Group, Massachusetts Institute of Technology, Cambridge, MA
02139-4307, USA*

[¶]*Department of Chemistry, Massachusetts Institute of Technology, Cambridge, MA
02139-4307, USA*

[§]*Department of Electrical Engineering and Computer Science, Massachusetts Institute of
Technology, Cambridge, MA 02139-4307, USA*

^{||}*Department of Nuclear Science and Engineering, Massachusetts Institute of Technology,
Cambridge, MA 02139-4307, USA*

E-mail: nguyen.tuan.hung.e4@tohoku.ac.jp; mingda@mit.edu

Contents

1	Dataset for training GNNOpt model	2
2	Performance of GNNOpt for optical prediction	5
2.1	Accuracy of model	5
2.2	Scalability of model	12
3	Dataset for unseen materials	13
4	GNNOpt for $\alpha(\omega)$ with $0 < \hbar\omega < 10$ eV	14
5	Surface state Fermi map of SiOs	16
6	Tables of the candidates	17
6.1	High-SMLE materials for solar cell	17
6.2	High-quantum-weight quantum material	22

1 Dataset for training GNNOpt model

The data set for training the GNNOpt model includes 944 materials obtained from the Materials Project. The distribution of the number of atoms per unit cell, lattice parameters, and energy band gap is plotted in Figure S1. The distribution of the training, validation, and testing datasets is plotted in Figure S2. In Figure S3, the original DFT data is interpolated into 251 points ranging from 0 to 50 eV by using NumPy.linspace() function.

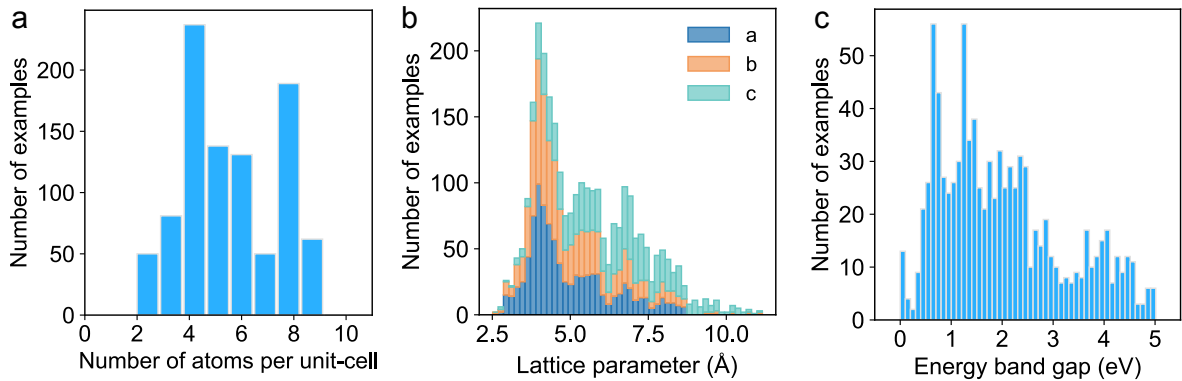


Figure S1: The distribution of (a) the number of atoms per unit cell, (b) the lattice parameters, and (c) the energy band gap. The total 944 materials from the Materials Project contain 2 to 9 atoms per unit cell and the energy band gap from 0 to 5 eV.

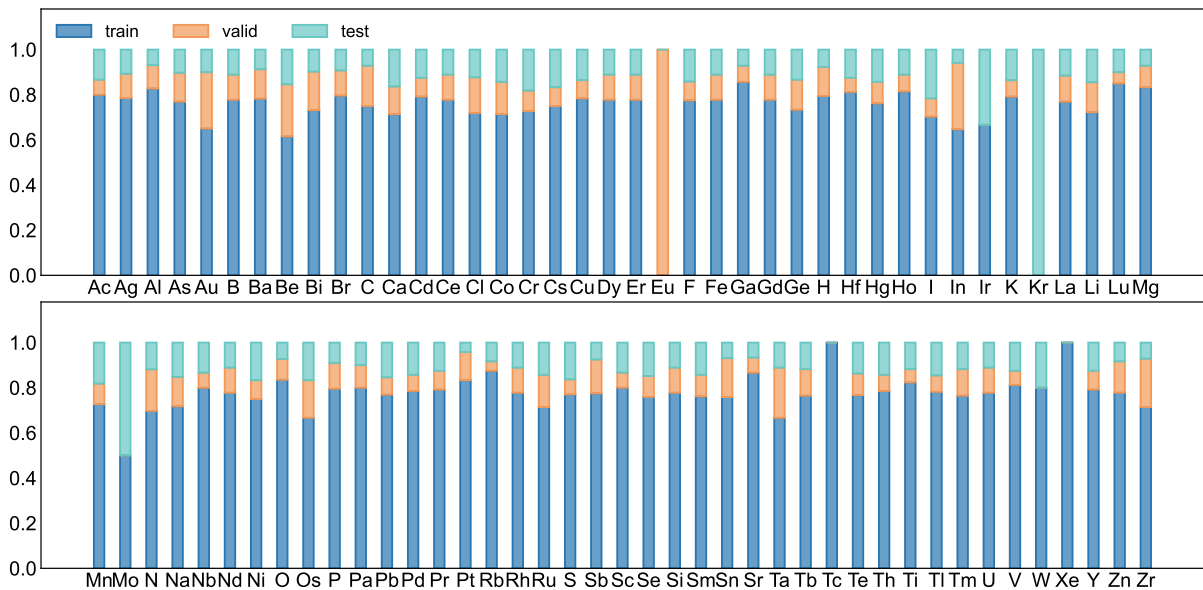


Figure S2: The distribution of the training, validation, and testing data by elements, in which the data is randomly split into 80%, 10%, and 10%, respectively.

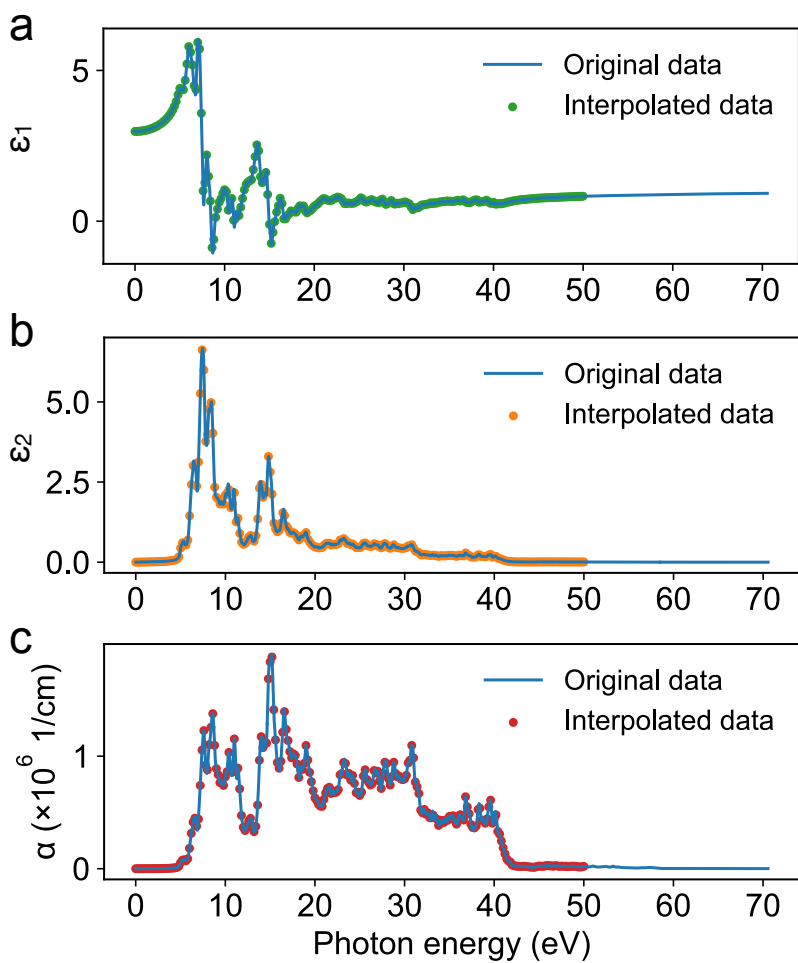


Figure S3: Interpolation data with 251 points ranging from 0 to 50 eV from the original DFT spectra (solid lines). (a) The real ϵ_1 , (b) imaginary ϵ_2 parts of the dielectric function, and (c) the absorption coefficient α are plotted as a function of the photon energy.

2 Performance of GNNOpt for optical prediction

2.1 Accuracy of model

We show the loss history of the trained GNNOpt model as a function of epoch number in Figure S4 and the direct optical prediction of training, validation, and testing datasets in Figures S5-S10 for the real ϵ_1 and imaginary ϵ_2 parts of the dielectric function, absorption coefficient α , real n and imaginary k parts of refractive index, and reflectance R , respectively.

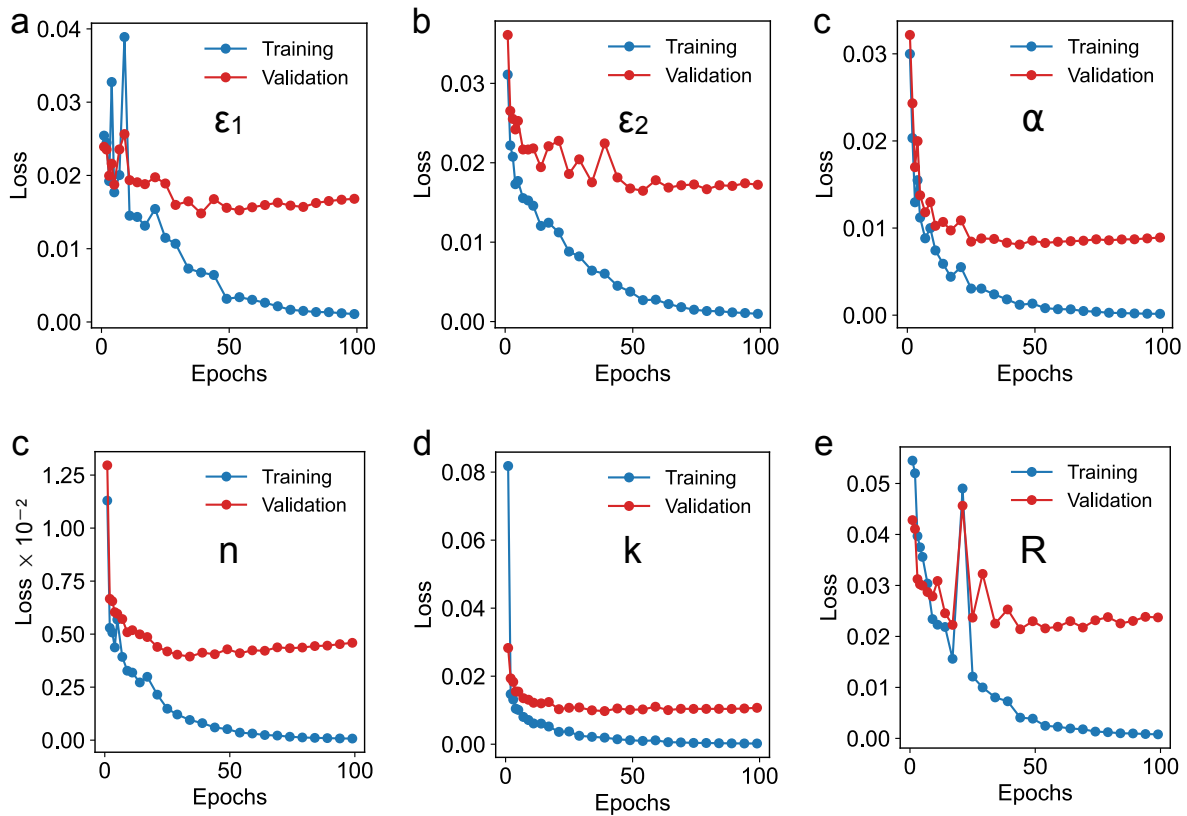


Figure S4: Loss history as a function of epoch number for the (a) real ϵ_1 and (b) imaginary ϵ_2 parts of the dielectric function, (c) absorption coefficient α , (d) real n and (e) imaginary k parts of refractive index, and (f) reflectance R .

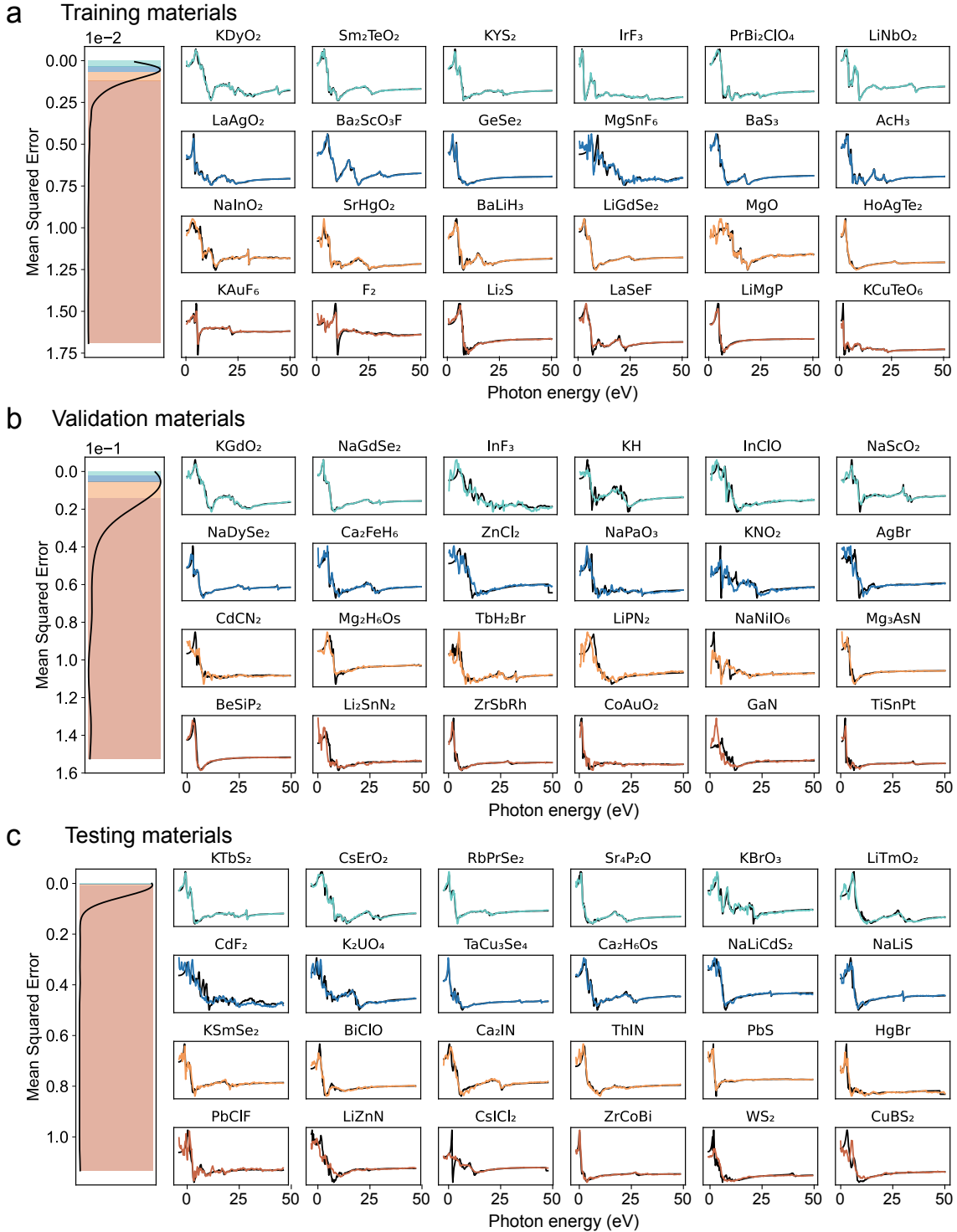


Figure S5: Direct prediction results for real ϵ_1 part of the dielectric function of training, validation, and testing datasets. Color lines are the GNNOpt-predicted spectra, and black lines are the DFT ground-truth spectra. 24 random materials are selected for each dataset, and the selected materials correspond to each error quartile in the mean squared error distribution (left figure) with the same color.

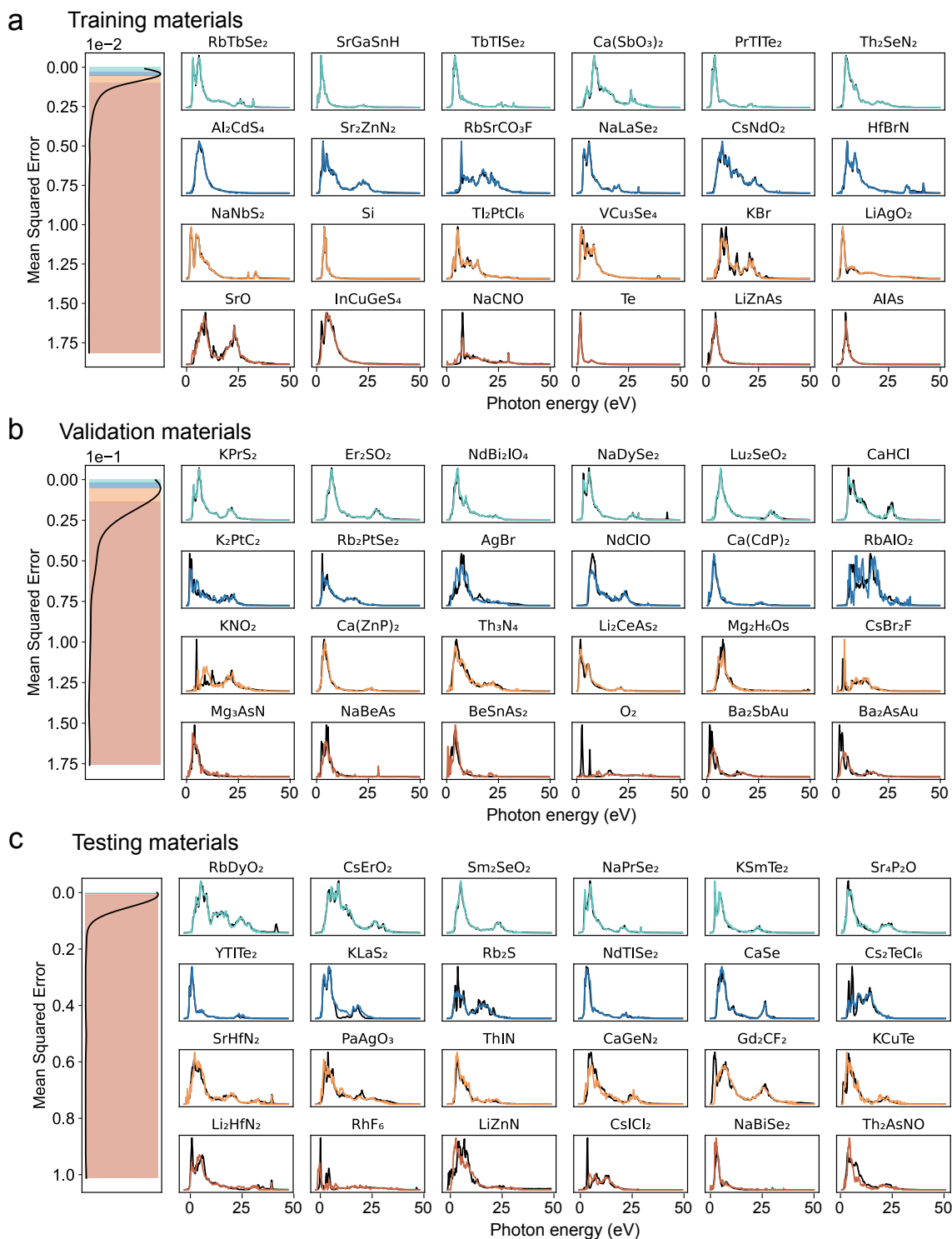


Figure S6: Direct prediction results for imaginary ϵ_2 part of the dielectric function of training, validation, and testing datasets. Color lines are the GNNOpt-predicted spectra, and black lines are the DFT ground-truth spectra. 24 random materials are selected for each dataset, and the selected materials correspond to each error quartile in the mean squared error distribution (left figure) with the same color.

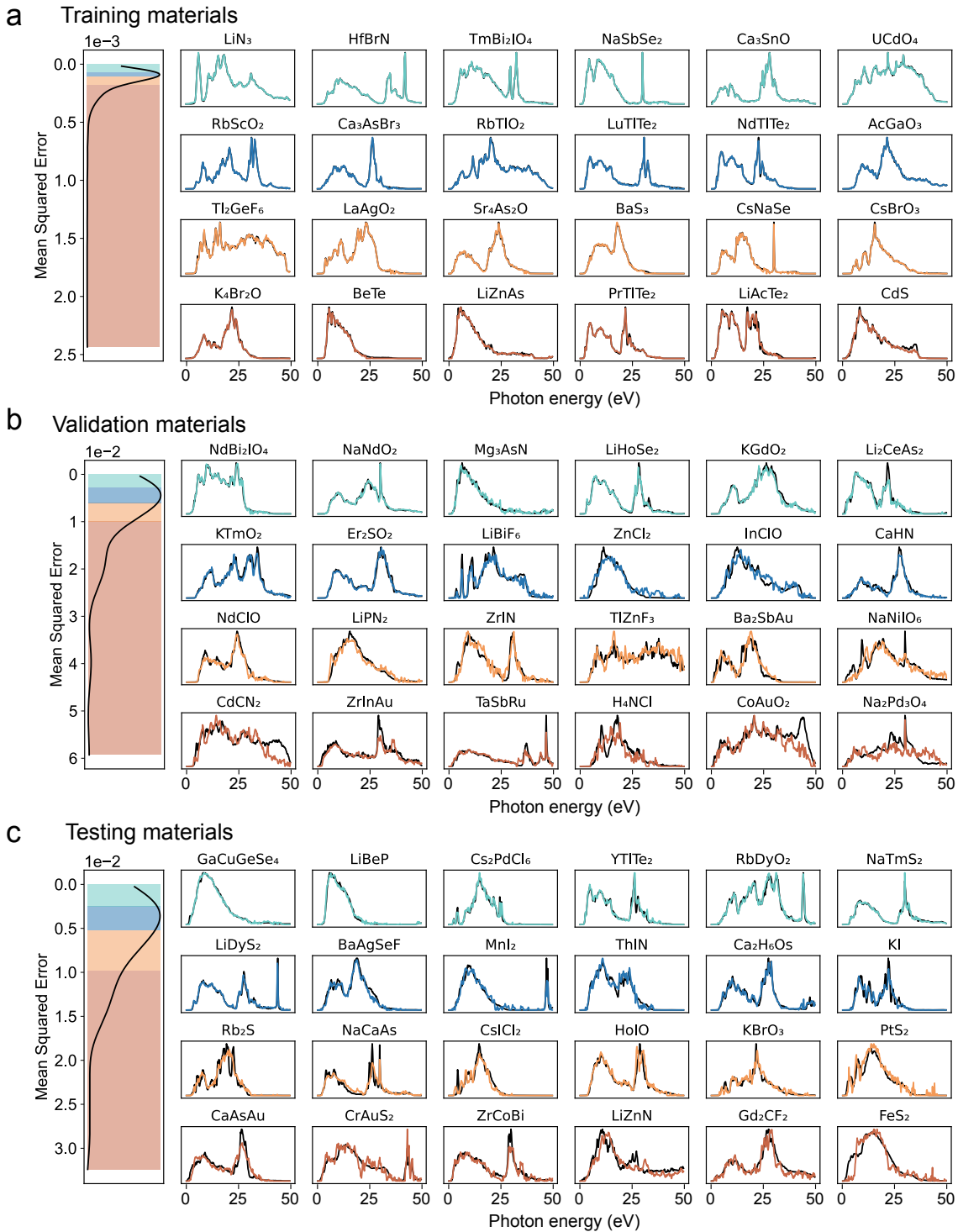


Figure S7: Direct prediction results for absorption coefficient α of training, validation, and testing datasets. Color lines are the GNNOpt-predicted spectra, and black lines are the DFT ground-truth spectra. 24 random materials are selected for each dataset, and the selected materials correspond to each error quartile in the mean squared error distribution (left figure) with the same color.

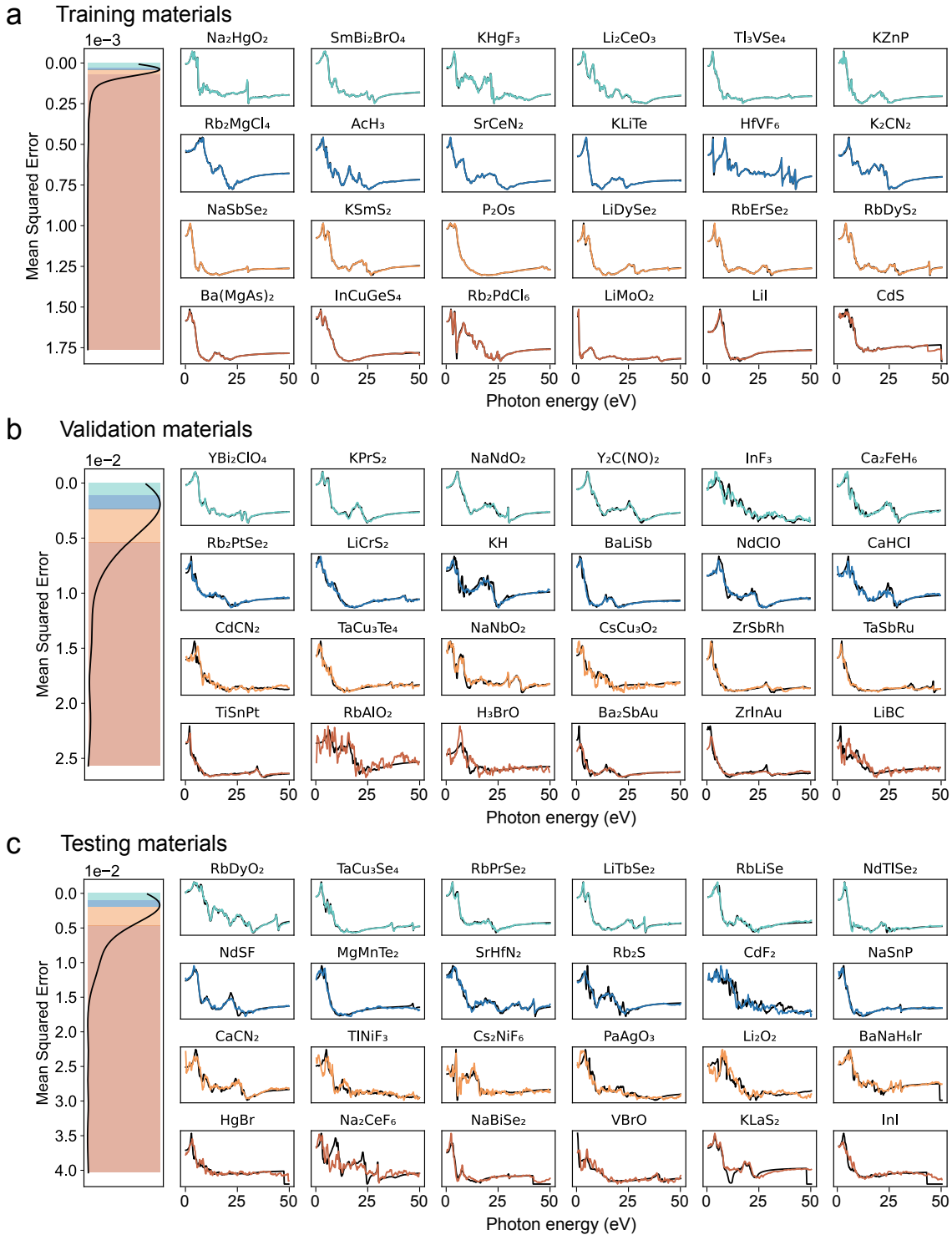


Figure S8: Direct prediction results for real n part of the refractive index of training, validation, and testing datasets. Color lines are the GNNOpt-predicted spectra, and black lines are the DFT ground-truth spectra. 24 random materials are selected for each dataset, and the selected materials correspond to each error quartile in the mean squared error distribution (left figure) with the same color.

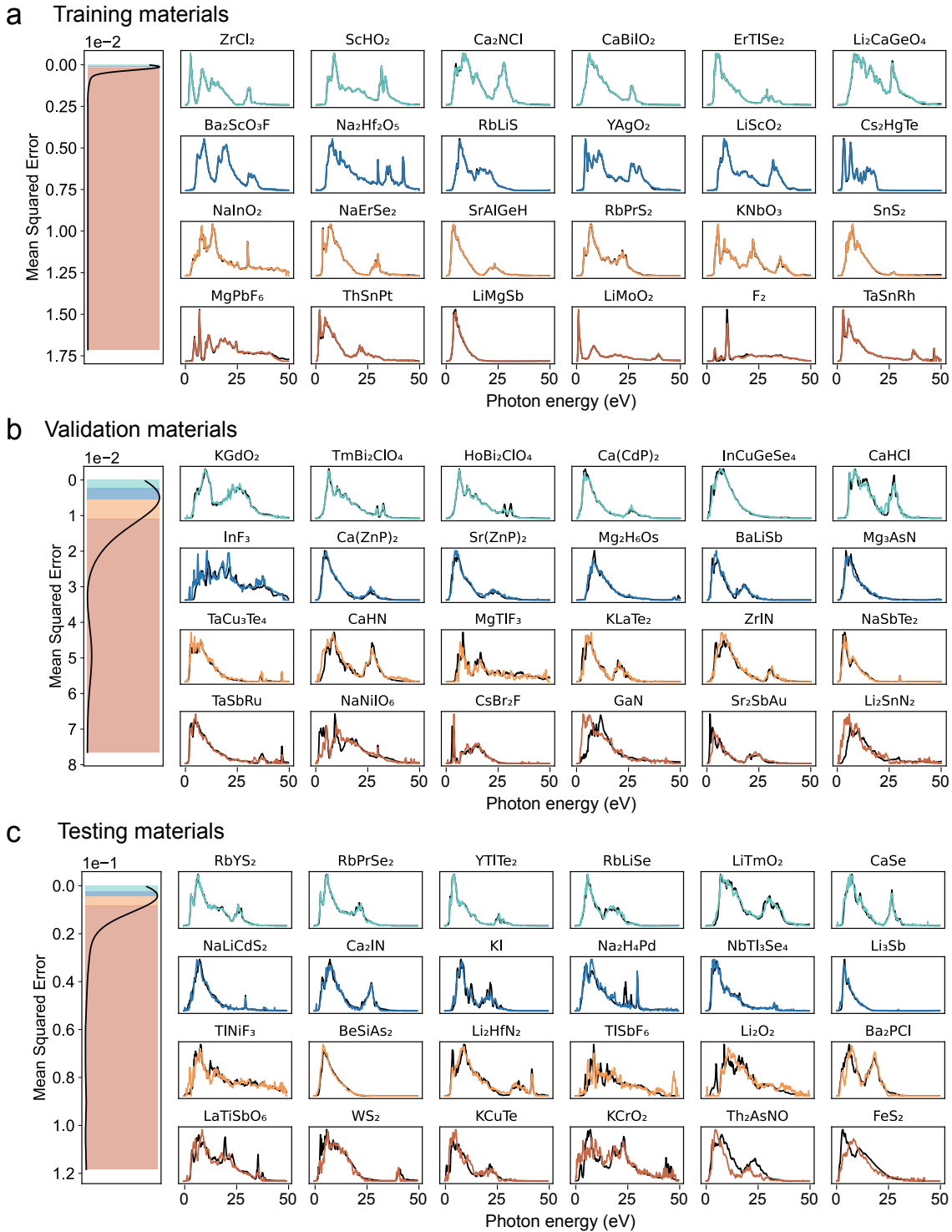


Figure S9: Direct prediction results for imaginary k part of the refractive index of training, validation, and testing datasets. Color lines are the GNNOpt-predicted spectra, and black lines are the DFT ground-truth spectra. 24 random materials are selected for each dataset, and the selected materials correspond to each error quartile in the mean squared error distribution (left figure) with the same color.

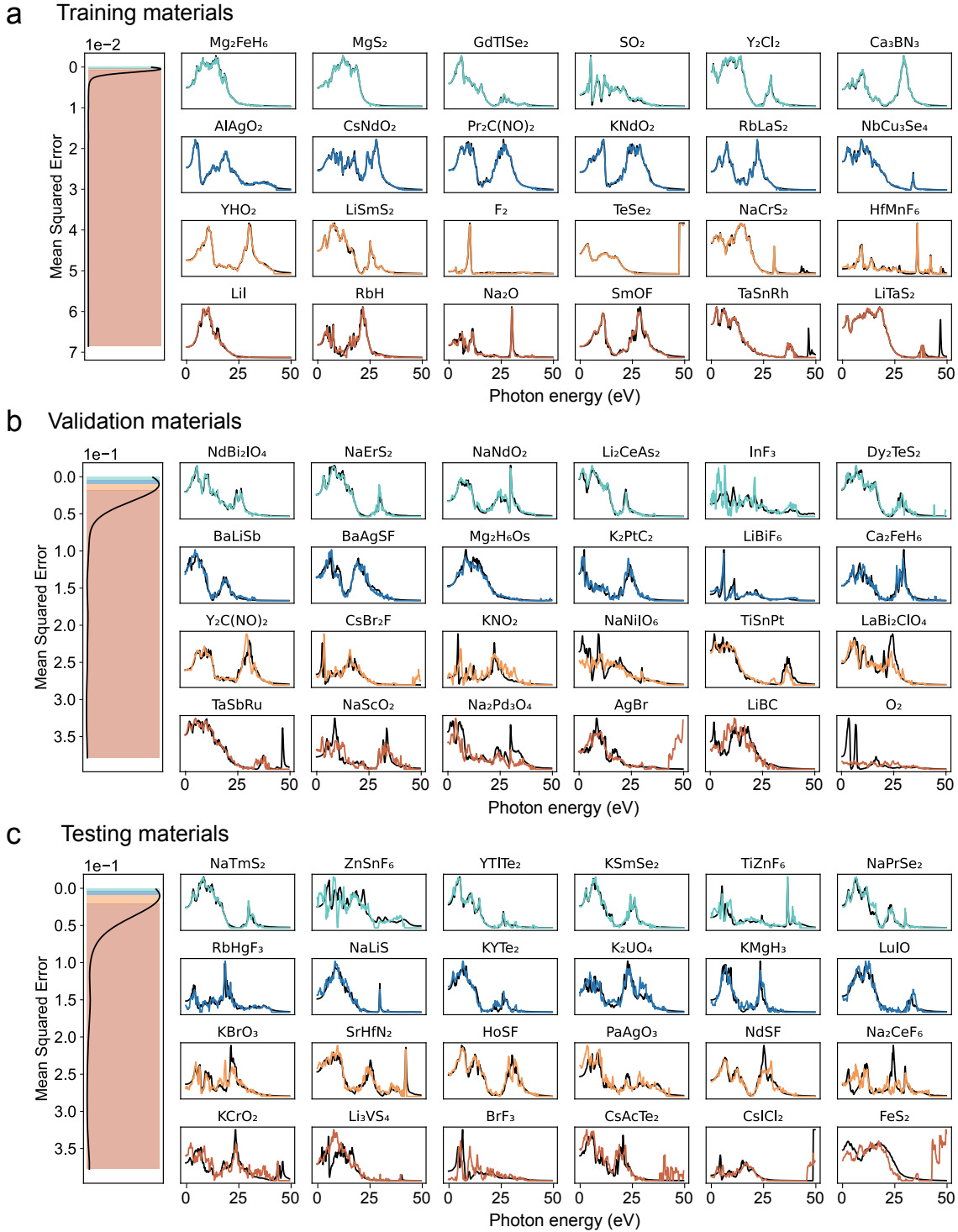


Figure S10: Direct prediction results for reflectance R of training, validation, and testing datasets. Color lines are the GNNOpt-predicted spectra, and black lines are the DFT ground-truth spectra. 24 random materials are selected for each dataset, and the selected materials correspond to each error quartile in the mean squared error distribution (left figure) with the same color.

2.2 Scalability of model

Figure S11 shows the performance of the GNNOpt for three cases with the different testing sets, including the atomic site numbers $N_{\text{test}} = 8, 9$ (case I), $N_{\text{test}} = 7, 8, 9$ (case II), and $N_{\text{test}} = 6, 7, 8, 9$ (case III). Since $N_{\text{train}} < N_{\text{test}}$ for three cases, the GNNOpt shows the scalability to predict the unseen materials, which have a larger number of atoms per unit cell than the training dataset.

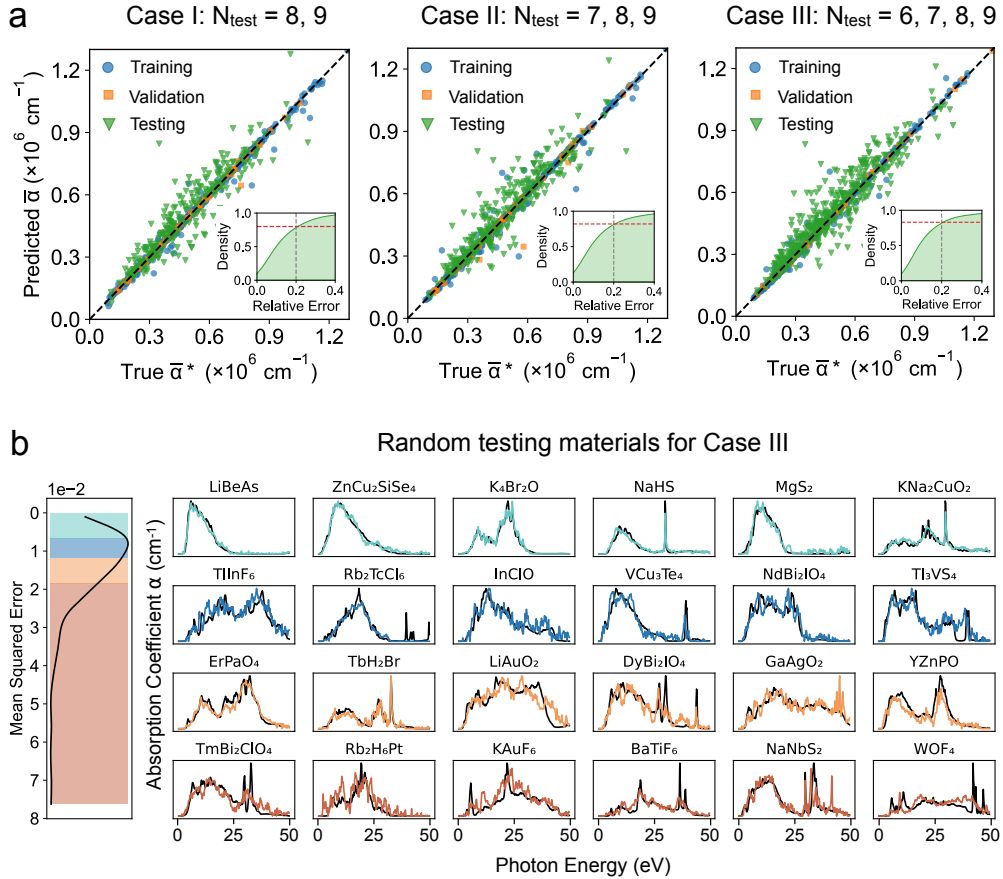


Figure S11: (a) Correlation plots for three cases (I, II, III), which correspond to three GNNOpt models with the testing dataset, including the atomic site numbers $N_{\text{test}} = 8, 9$, $N_{\text{test}} = 7, 8, 9$, and $N_{\text{test}} = 6, 7, 8, 9$, respectively. The circle, square, and triangle symbols denote the training, validation, and testing datasets, respectively. The inset figures show the distribution of the relative error. (b) Direct prediction results for absorption coefficient α of a testing dataset of case III. Color lines are the GNNOpt-predicted spectra, and black lines are the DFT ground-truth spectra. 24 random materials are selected for each dataset, and the selected materials correspond to each error quartile in the mean squared error distribution (left figure) with the same color.

3 Dataset for unseen materials

The data set for unseen materials is obtained from the Materials Project, which includes 5,281 stable insulators (i.e., energy above hull ≥ 0 eV/atom) and contains 2 to 19 atoms per unit cell and the energy band gap from 0 to 5 eV. The distribution of the number of atoms per unit cell, lattice parameters, and energy band gap is plotted in Figure S12.

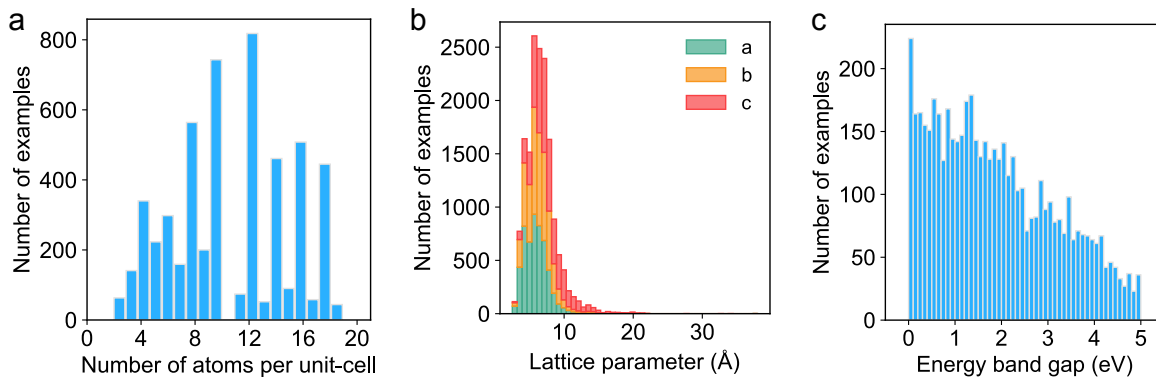


Figure S12: The distribution of (a) the number of atoms per unit cell, (b) the lattice parameters, and (c) the energy band gap. The total 5,281 stable materials from the Materials Project contain 2 to 19 atoms per unit cell and the energy band gap from 0 to 5 eV.

4 GNNOpt for $\alpha(\omega)$ with $0 < \hbar\omega < 10$ eV

In order to increase the resolution of the optical spectra ranging from 0 to 10 eV for the solar cell application. We retrain the GNNOpt model with $0 < \hbar\omega < 10$ eV. In Figures S13a and b, we show the loss history and the correlation between the GNNOpt-predicted and DFT ground-truth, respectively. $R^2 = 0.95$ for the testing set, and the relative error below for the testing set 10% is 78%.

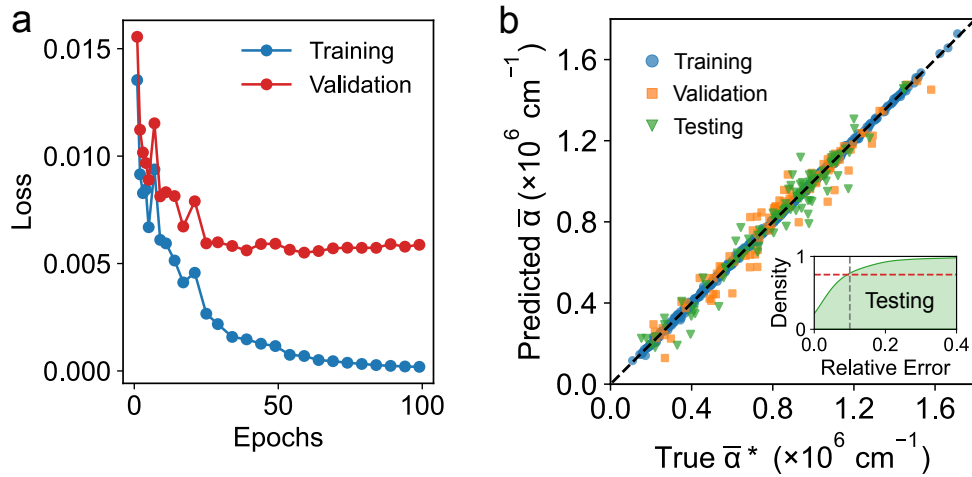


Figure S13: (a) Loss history as a function of epoch number, and (b) correlation plots of training (blue circle), validation (square orange), and testing (triangle green) datasets. The inset figures show the distribution of the relative error.

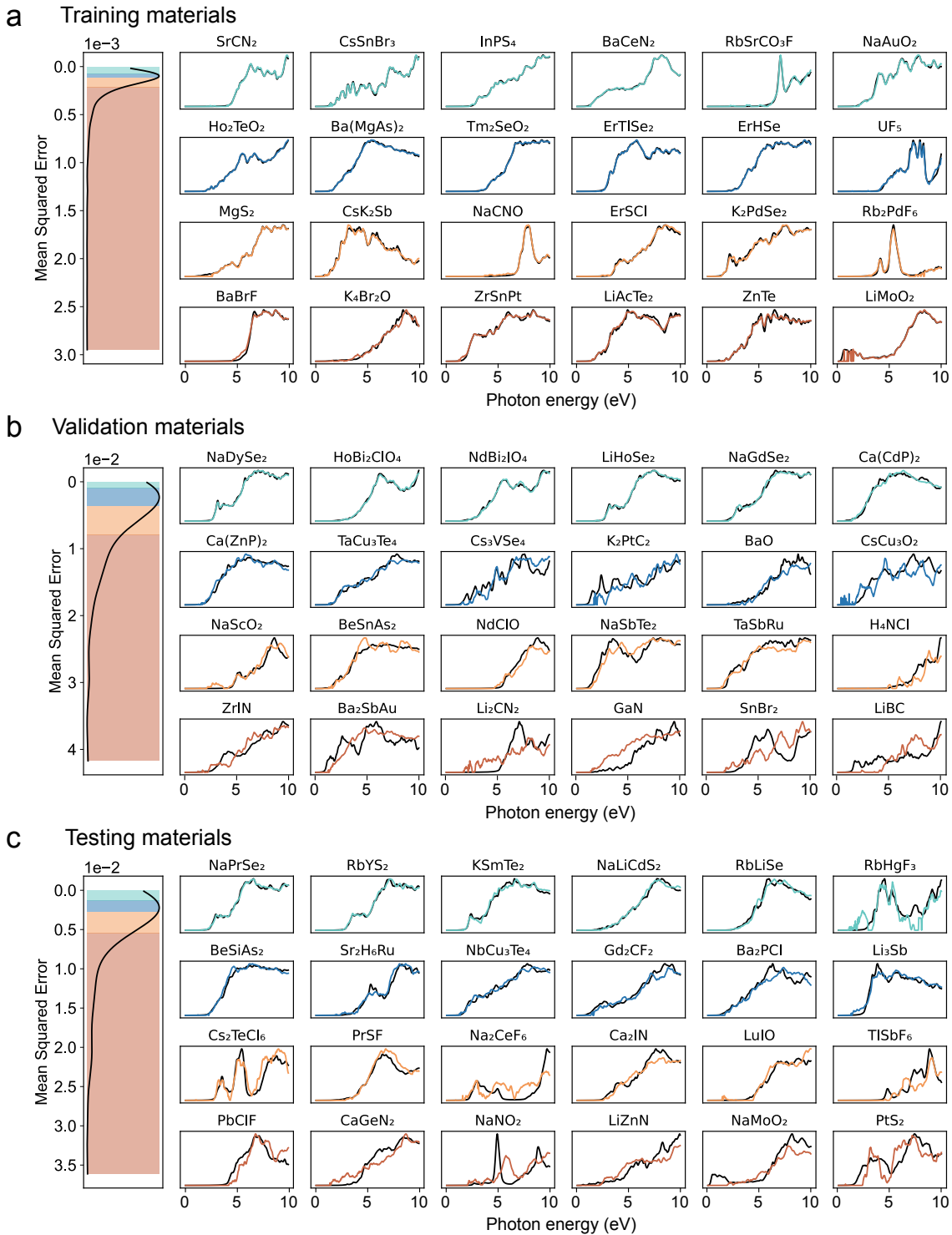


Figure S14: Direct prediction results for absorption coefficient α of training, validation, and testing datasets. Color lines are the GNNOpt-predicted spectra, and black lines are the DFT ground-truth spectra. 24 random materials are selected for each dataset, and the selected materials correspond to each error quartile in the mean squared error distribution (left figure) with the same color.

5 Surface state Fermi map of SiOs

In order to check the trivial or nontrivial surface state on the (001) surface of SiOs, we plot the Fermi maps in Figure S15.

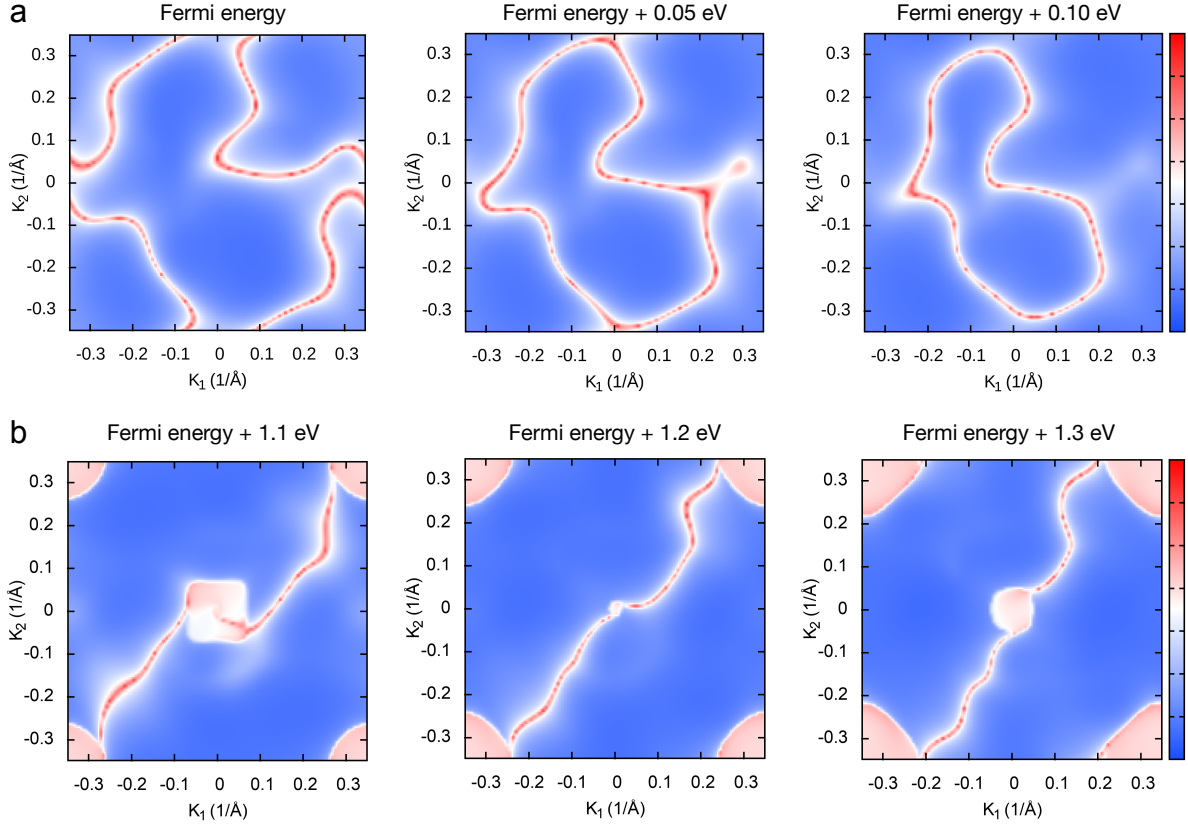


Figure S15: Surface state Fermi map of SiOs taken at (a) Fermi energy E_F , $E_F + 0.05$ eV, $E_F + 0.1$ eV and (b) $E_F + 1.10$, $E_F + 1.2$ eV, and $E_F + 0.13$ eV. The color bar scale is in arbitrary units. The trivial surface is found near the Fermi level with the closed loops, while the nontrivial topological surface is located around $E_F + 1.2$ eV with the Fermi arcs.

6 Tables of the candidates

Tables S1 and S2 list the material candidates for the solar cell and the quantum materials, respectively. By using the MP-ID column, one can find the detailed structure from the Materials Project website. In Table S1, we list only the materials with the solar cell efficiency $\eta > 32\%$, in which η is evaluated by using the spectroscopic limited maximum efficiency (SLME) approach. In Table S1, we list only the materials with the quantum weight $K_{xx} > 28.87$, in which $K_{xx} = 28.87$ is the quantum weight of the well-known topology insulator Bi_2Te_3 .

6.1 High-SMLE materials for solar cell

Table S1: The list of 246 high- η materials with the Materials Project IDs (MP-ID). The solar cell efficiency η (the spectroscopic limited maximum efficiency) in the unit of % and the energy band gap E_g in the unit of eV.

MP-ID	Formula	E_g	η	MP-ID	Formula	E_g	η
mp-861942	Ag ₂ GePbS ₄	1.370	32.918	mp-7439	K ₃ Cu ₃ P ₂	1.289	32.251
mp-556866	Ag ₂ HgSI ₂	1.221	32.389	mp-9273	K ₃ Sb ₂ Au ₃	1.105	32.155
mp-36216	Ag ₂ S	1.296	32.347	mp-8704	K ₃ SbSe ₄	1.432	32.275
mp-29163	Ag ₂ TeS ₃	1.300	32.399	mp-1223443	KBiS ₂	1.416	32.126
mp-6215	AgHgAsS ₃	1.245	32.115	mp-20076	KCrF ₆	1.398	32.128
mp-560067	AgHgSBr	1.260	32.103	mp-4026	KCrS ₂	1.164	32.598
mp-23140	AgHgSI	1.358	32.923	mp-9263	KErTe ₂	1.330	32.720
mp-580941	AgI	1.376	32.797	mp-23582	KLi ₆ BiO ₆	1.422	32.053
mp-3922	AgSbS ₂	1.372	32.894	mp-7089	KMgSb	1.267	32.141
mp-2624	AlSb	1.226	32.400	mp-6599	KNb(CuSe ₂) ₂	1.423	32.442

Continued on next page

Continued from previous page

mp-31220	AlSiTe3	1.250	32.178	mp-11740	KNdTe2	1.265	32.179
mp-1214793	AsOsS	1.180	32.580	mp-5273	KPrTe2	1.280	32.180
mp-1228745	AsRhS	1.224	32.439	mp-9576	KSbSe2	1.130	32.579
mp-505373	AsSeI	1.235	32.372	mp-9036	KSmTe2	1.262	32.175
mp-7374	Ba(CuO)2	1.386	32.837	mp-1188829	KTeP2	1.209	32.474
mp-8278	Ba(MgP)2	1.137	32.430	mp-16763	KYTe2	1.298	32.316
mp-1104988	Ba2Bi2Se3O2	1.419	32.483	mp-4841	LaCuS2	1.235	32.085
mp-21879	Ba2CePtO6	1.420	32.274	mp-989524	LaWN3	1.210	32.111
mp-11902	Ba2GeSe4	1.412	32.482	mp-28989	Li10BrN3	1.367	32.778
mp-864638	Ba2InBiS5	1.453	32.003	mp-8181	Li2CeN2	1.204	32.518
mp-14448	Ba2SiTe4	1.103	32.059	mp-675779	Li2Mo3S4	1.437	32.256
mp-1104423	Ba2YAg5S6	1.366	32.625	mp-7608	Li2PdO2	1.197	32.360
mp-19913	Ba3(InP2)2	1.109	32.295	mp-22170	Li4PbO4	1.437	32.221
mp-510268	Cs2Pd3S4	1.382	32.905	mp-29365	Li5BiO5	1.360	32.142
mp-14338	Cs2Pt3Se4	1.333	32.943	mp-765559	LiAgF4	1.128	32.226
mp-505825	Cs2PtC2	1.270	32.146	mp-996959	LiAuO2	1.306	32.300
mp-540957	Cs2TeI6	1.388	32.872	mp-31468	LiCaN	1.378	32.834
mp-10489	Cs2Ti(CuSe2)2	1.364	32.423	mp-1211088	LiCaP	1.399	32.516
mp-3247	Cs2TiS3	1.272	32.111	mp-1207082	LiMgSb	1.444	32.123
mp-1112112	Cs2TlAsBr6	1.305	32.458	mp-1029903	LiNbN2	1.142	32.257
mp-8684	Cs2VAgS4	1.387	32.696	mp-850189	LiVSnO4	1.452	32.070
mp-9856	Cs2ZrSe3	1.369	32.197	mp-10182	LiZnP	1.339	32.681
mp-505212	Cs3AuO	1.326	32.832	mp-1029378	Mg2SbN3	1.358	32.718

Continued on next page

Continued from previous page

mp-1096933	CsAgO2	1.106	32.028	mp-5942	NaAsS2	1.355	32.182
mp-567913	CsAuSe3	1.192	32.556	mp-23110	NaHg2IO2	1.388	32.335
mp-553303	CsCu3O2	1.457	32.008	mp-3744	NaNbO2	1.378	32.631
mp-510462	CsDyZnTe3	1.371	32.426	mp-559446	NaPPdS4	1.161	32.608
mp-569107	CsErZnTe3	1.386	32.198	mp-8830	NaRhO2	1.377	32.889
mp-579556	CsHoZnTe3	1.377	32.520	mp-999447	NaSmTe2	1.174	32.432
mp-11124	CsLaHgSe3	1.455	32.029	mp-13275	NaSrP	1.236	32.247
mp-34034	Ba8P5Br	1.164	32.624	mp-5475	NaTaN2	1.276	32.105
mp-9195	BaCuSeF	1.427	32.163	mp-1180119	NaTiCu3Se4	1.371	32.894
mp-28007	BaHgS2	1.157	32.229	mp-4043	NbCu3Se4	1.360	32.877
mp-1214348	BaLaAgTe3	1.293	32.274	mp-1016197	MgSiAs2	1.303	32.007
mp-27251	Bi2TeO6	1.259	32.216	mp-2604	MgTe2	1.116	32.453
mp-33723	BiTeBr	1.236	32.304	mp-19442	Mn(Ni3O4)2	1.425	32.400
mp-22965	BiTeI	1.233	32.383	mp-19142	Mn2V2O7	1.204	32.210
mp-1078908	Ca2CdP2	1.293	32.279	mp-28013	MnI2	1.171	32.439
mp-1205338	Ca3(AlAs2)2	1.110	32.339	mp-1634	MoSe2	1.301	32.428
mp-1205337	Ca3(AlP2)2	1.248	32.276	mp-3622	Na2PdF4	1.139	32.453
mp-8789	Ca4As2O	1.213	32.457	mp-3527	Na3AgO2	1.144	32.343
mp-5380	Ca4P2O	1.271	32.169	mp-5122	Na3AlP2	1.346	32.727
mp-28879	Ca5P8	1.142	32.352	mp-28400	P3Ru	1.145	32.580
mp-1213950	CaAgAsO4	1.357	32.508	mp-1103842	P4Os	1.304	32.446
mp-1029633	CaSnN2	1.377	32.899	mp-27173	P4Ru	1.259	32.221
mp-4666	CdSiP2	1.426	32.353	mp-1219924	PRhS	1.399	32.737

Continued on next page

Continued from previous page

mp-19178	CoAgO ₂	1.332	32.949	mp-9798	Rb(SbSe ₂) ₂	1.119	32.499
mp-1226003	CoPS	1.123	32.533	mp-1111655	Rb ₂ AgAsCl ₆	1.295	32.155
mp-551407	CoSeO ₄	1.366	32.528	mp-1110602	Rb ₂ AgRhF ₆	1.390	32.612
mp-21074	Cr ₂ HgO ₄	1.258	32.223	mp-1205560	Rb ₂ As ₂ Pd	1.146	32.623
mp-21355	Cr ₂ TeO ₆	1.424	32.435	mp-1206059	Rb ₂ NaCrCl ₆	1.363	32.534
mp-996996	CrAuO ₂	1.266	32.199	mp-1205714	Rb ₂ P ₂ Pd	1.265	32.199
mp-8890	Cs(SbS ₂) ₂	1.441	32.209	mp-11695	Rb ₂ Pd ₃ S ₄	1.185	32.591
mp-3312	Cs(SbSe ₂) ₂	1.122	32.519	mp-28145	Rb ₂ PdCl ₆	1.287	32.203
mp-1113578	Cs ₂ AgAsBr ₆	1.116	32.412	mp-10919	Rb ₂ PtC ₂	1.136	32.607
mp-1106156	Cs ₂ Hg ₃ Se ₄	1.195	32.199	mp-8901	Rb ₂ VAgS ₄	1.332	32.777
mp-1096926	Cs ₂ InAgCl ₆	1.342	32.381	mp-15219	Rb ₂ VCuS ₄	1.244	32.164
mp-510065	CsNdHgSe ₃	1.354	32.775	mp-9718	Rb ₃ BA _s ₂	1.294	32.236
mp-11742	CsNdTe ₂	1.292	32.246	mp-9274	Rb ₃ Sb ₂ Au ₃	1.222	32.443
mp-12342	CsNdZnTe ₃	1.365	32.844	mp-8603	RbAgO	1.417	32.273
mp-7211	CsPrHgSe ₃	1.337	32.836	mp-30041	RbBiS ₂	1.339	32.409
mp-12341	CsPrZnTe ₃	1.361	32.811	mp-9845	RbCaAs	1.299	32.385
mp-2969	CsSbSe ₂	1.131	32.582	mp-5808	RbNdTe ₂	1.299	32.364
mp-7212	CsSmHgSe ₃	1.363	32.852	mp-616564	RbPbIO ₆	1.375	32.893
mp-12343	CsSmZnTe ₃	1.409	32.570	mp-999269	RbSmTe ₂	1.316	32.610
mp-1542038	CsSnSe ₃	1.190	32.344	mp-9008	RbTeAu	1.108	32.155
mp-638078	CsTbZnTe ₃	1.357	32.619	mp-16764	RbYTe ₂	1.356	32.816
mp-1541909	CsTeAu	1.416	32.543	mp-28918	Sb ₂ WO ₆	1.189	32.103
mp-1205877	CsTlO	1.391	32.556	mp-11178	SrCeN ₂	1.268	32.198

Continued on next page

Continued from previous page

mp-1103187	CsTmZnTe3	1.384	32.242	mp-13276	SrLiP	1.343	32.859
mp-11123	CsYHgSe3	1.395	32.705	mp-1542758	SrMoO3	1.309	32.156
mp-1103744	CsYZnTe3	1.405	32.475	mp-1029275	SrZrN2	1.227	32.414
mp-1025340	Cu2WSe4	1.276	32.199	mp-9295	TaCu3Te4	1.141	32.597
mp-1225724	Dy(CuS)3	1.397	32.764	mp-1217848	Tb(CuS)3	1.341	32.942
mp-1095296	Dy4Te3S4	1.397	32.740	mp-30291	Tb4Se3N2	1.345	32.318
mp-1181462	DyAgSe2	1.306	32.049	mp-5737	TbCuS2	1.183	32.528
mp-1225120	Er(CuS)3	1.446	32.155	mp-9481	TcS2	1.189	32.435
mp-1189719	Er3Tl2Cu5S8	1.283	32.197	mp-27741	TeAuI	1.121	32.518
mp-22421	Fe2GeO4	1.408	32.472	mp-1217271	Th2PNO	1.313	32.545
mp-35596	Fe2NiO4	1.362	32.772	mp-1079673	ThSe3	1.273	32.019
mp-19225	FeAgO2	1.148	32.417	mp-29091	Ti(CuS)4	1.426	32.411
mp-30946	Ga2PdI8	1.418	32.494	mp-29337	Tl3BS3	1.422	32.188
mp-541785	GePdS3	1.344	32.944	mp-28490	Tl3BSe3	1.225	32.277
mp-2242	GeS	1.238	32.358	mp-8630	SbIrS	1.396	32.772
mp-29419	Hf(Te2Cl3)2	1.263	32.025	mp-1095507	SbIrSe	1.147	32.626
mp-985829	HfS2	1.224	32.260	mp-1102833	SbOsS	1.119	32.469
mp-554921	Hg(BiS2)2	1.186	32.113	mp-1101771	SbOsSe	1.123	32.518
mp-1224171	Hg11I2BrClO4	1.308	32.508	mp-1209072	SbSeBr	1.438	32.268
mp-28875	Hg2P3Cl	1.135	32.326	mp-22996	SbSeI	1.381	32.905
mp-23192	HgI2	1.332	32.915	mp-1094066	ScAgS2	1.238	32.114
mp-9006	Ho2CF2	1.136	32.584	mp-1206699	Si4P4Os	1.434	32.318
mp-27988	IF7	1.440	32.184	mp-1863	SiAs	1.452	32.082

Continued on next page

Continued from previous page

mp-22186	In ₆ Ge ₂ PtO ₉	1.345	32.905	mp-5081	SmCuS ₂	1.168	32.548
mp-1223929	InCuGeS ₄	1.135	32.121	mp-550820	SmZnPO	1.361	32.279
mp-2437	IrF ₃	1.141	32.616	mp-36381	Sn(PS ₃) ₂	1.194	32.053
mp-9797	K(SbSe ₂) ₂	1.117	32.474	mp-37091	Sr(AlTe ₂) ₂	1.445	32.156
mp-28769	K(SnSe ₂) ₂	1.173	32.605	mp-863260	Sr(MgAs) ₂	1.346	32.462
mp-9778	K ₂ AgP	1.232	32.377	mp-1986938	Sr ₂ Bi ₂ Se ₃ O ₂	1.387	32.825
mp-7643	K ₂ AgSb	1.187	32.586	mp-1208839	Sr ₂ H ₆ Pt	1.276	32.204
mp-1110871	K ₂ CuBiCl ₆	1.162	32.627	mp-1189305	Sr ₃ (AlAs ₂) ₂	1.146	32.614
mp-8446	K ₂ CuP	1.142	32.414	mp-9843	Sr ₃ (AlP ₂) ₂	1.337	32.972
mp-1206266	K ₂ NaCrCl ₆	1.388	32.263	mp-8299	Sr ₄ As ₂ O	1.192	32.530
mp-23067	K ₂ PdCl ₆	1.203	32.191	mp-8298	Sr ₄ P ₂ O	1.213	32.427
mp-1068941	K ₂ PdS ₂	1.117	32.229	mp-676540	TlSbS ₂	1.267	32.171
mp-1062676	K ₂ Pt	1.315	32.170	mp-1821	WSe ₂	1.447	32.157
mp-8235	K ₂ SiP ₂	1.209	32.262	mp-1216184	Y(CuS) ₃	1.420	32.502
mp-8965	K ₂ Sn ₂ S ₅	1.406	32.509	mp-1188559	YAgSe ₂	1.280	32.144
mp-8900	K ₂ VAgS ₄	1.305	32.285	mp-35311	ZnCrF ₆	1.246	32.298
mp-15147	K ₂ VCuS ₄	1.234	32.213	mp-1215793	ZnCrFeO ₄	1.323	32.260
mp-15220	K ₂ VCuSe ₄	1.125	32.531	mp-4524	ZnGeP ₂	1.178	32.533
mp-14206	K ₃ Ag ₃ As ₂	1.253	32.257	mp-13983	ZnPdF ₆	1.357	32.892
mp-28347	K ₃ Al ₂ As ₃	1.186	32.425	mp-541912	ZrBrN	1.442	32.206
mp-14205	K ₃ Cu ₃ As ₂	1.274	32.206	mp-1100415	ZrSbRh	1.165	32.628

6.2 High-quantum-weight quantum material

Table S2: The list of 296 high-quantum-weight K_{xx} materials with the Materials Project IDs (MP-ID). K_{xx} in unit of h/e^2 and the energy band gap E_g in the unit of eV.

MP-ID	Formula	E_g	K_{xx}	MP-ID	Formula	E_g	K_{xx}
mp-10910	Al2Ru	0.086	28.617	mp-1219954	NiSb6Ru	0.068	32.614
mp-1228817	AlReGe	0.119	35.783	mp-1209793	Np(FeP3)4	0.480	33.162
mp-1228809	AlReSi	0.047	29.443	mp-10155	P2Ir	0.633	46.937
mp-15649	As2Ir	0.816	44.405	mp-2319	P2Os	0.890	40.052
mp-2455	As2Os	0.665	39.786	mp-28266	P2Pd	0.342	32.287
mp-2513	As2Pt	0.079	34.342	mp-730	P2Pt	1.019	33.680
mp-15954	As2Rh	0.263	38.237	mp-15953	P2Rh	0.370	39.380
mp-766	As2Ru	0.449	39.648	mp-1413	P2Ru	0.479	38.024
mp-540912	As3Ir	0.027	40.000	mp-13853	P3Ir	0.085	38.772
mp-1228823	AsIrS	1.863	42.819	mp-28400	P3Ru	1.145	33.822
mp-1228810	AsIrSe	1.470	44.948	mp-1103842	P4Os	1.304	35.341
mp-1214793	AsOsS	1.180	38.644	mp-27173	P4Ru	1.259	33.051
mp-1214784	AsOsSe	1.003	40.793	mp-1220004	PIrS	1.865	39.670
mp-1228745	AsRhS	1.224	36.956	mp-1102534	POsS	0.944	32.364
mp-1228724	AsRhSe	0.914	39.136	mp-1219924	PRhS	1.399	33.787
mp-1214786	AsRuS	0.915	37.758	mp-1102531	PRhSe	1.083	38.673
mp-160	B	1.433	28.929	mp-2201	PbSe	0.426	28.452
mp-1227860	BaPPd	0.296	35.169	mp-1206667	PrNiBi	0.334	30.592
mp-1009084	BeSnAs2	0.694	28.774	mp-999305	PrRh	0.176	31.660
mp-675543	Bi2PbSe4	0.455	28.749	mp-1209288	PrTeAs	0.124	28.508
mp-27910	Bi2Te2S	0.437	38.461	mp-288	PtS	0.385	29.370

Continued on next page

Continued from previous page

mp-29666	Bi ₂ Te ₂ Se	0.544	36.650	mp-1115	PtSe ₂	0.619	28.405
mp-1102836	BiIrS	0.689	45.857	mp-1219672	Rb(Nb ₃ Se ₄) ₂	0.399	30.326
mp-1103228	BiIrSe	0.535	46.385	mp-17401	Rb ₃ Sn ₄ Au	0.581	36.759
mp-1103098	BiRhS	0.340	37.728	mp-5222	ReTeS	0.075	31.941
mp-1101765	BiRhSe	0.238	38.730	mp-1922	RuSe ₂	0.314	32.891
mp-1095302	BiSe ₂	0.672	27.910	mp-1247	Sb ₂ Ir	0.510	41.249
mp-1227426	BiTeRh	0.162	36.360	mp-2695	Sb ₂ Os	0.345	36.534
mp-11918	Ca(BeN) ₂	2.077	28.484	mp-20928	Sb ₂ Ru	0.003	37.206
mp-11168	Ca(PIr) ₂	0.494	36.158	mp-3525	Sb ₂ Te ₂ Se	0.131	53.130
mp-866229	Ca ₂ SnHg	0.149	29.260	mp-1201	Sb ₂ Te ₃	0.131	37.118
mp-31149	Ca ₃ BiN	0.369	30.271	mp-8612	Sb ₂ TeSe ₂	0.486	42.499
mp-989590	Ca ₆ Sn ₂ NF	0.132	30.401	mp-867249	TaAlFe ₂	0.324	37.970
mp-756301	Cd(CoO ₂) ₂	0.293	30.160	mp-12561	TaAs ₂	0.013	37.663
mp-1021508	Ce(As ₃ Ru) ₄	0.238	43.599	mp-867507	TaGaFe ₂	0.060	39.826
mp-1188930	Ce(BOs) ₄	0.227	35.037	mp-31454	TaSbRu	0.665	37.112
mp-1021509	Ce(FeAs ₃) ₄	0.147	46.688	mp-1100408	TaSnRh	1.059	36.916
mp-16272	Ce(FeP ₃) ₄	0.521	41.533	mp-28691	TaTe ₄ I	0.563	31.268
mp-1181682	Ce(FeSb ₃) ₄	0.231	41.049	mp-1206686	TbNiBi	0.230	29.679
mp-38564	Ce(Mo ₃ S ₄) ₂	0.338	38.439	mp-3716	TbNiSb	0.331	29.431
mp-1021505	Ce(P ₃ Os) ₄	0.283	39.770	mp-16313	TbSbPt	0.097	28.091
mp-10069	Ce(P ₃ Ru) ₄	0.192	38.990	mp-28029	TcP ₃	0.451	34.375
mp-1105726	Ce(Sb ₃ Os) ₄	0.051	41.596	mp-19	Te	0.186	36.109
mp-1189811	Ce(Sb ₃ Ru) ₄	0.043	38.882	mp-602	Te ₂ Mo	0.863	60.792

Continued on next page

Continued from previous page

mp-1069558	Ce ₂ SeN ₂	0.948	28.008	mp-267	Te ₂ Ru	0.285	47.772
mp-10478	CeAsRh	0.026	39.711	mp-484	Te ₃ As ₂	0.433	32.130
mp-1213954	CeBiRh	0.014	36.873	mp-1217418	Te ₄ Mo ₂ Ru	0.250	42.626
mp-1226908	CeCuGeH	0.201	38.067	mp-29190	Te ₄ MoBr	0.858	43.505
mp-1076951	CeNiGe	0.057	39.243	mp-1217272	TeAsIr	1.085	49.334
mp-2109	CePt ₂	0.009	47.908	mp-1095634	TeAsRu	0.825	45.580
mp-19178	CoAgO ₂	1.332	31.229	mp-19717	TePb	0.806	31.044
mp-2715	CoAs ₂	0.172	39.226	mp-22945	TeRhCl	0.780	34.465
mp-14285	CoP ₂	0.438	37.981	mp-1217322	TeSe	0.706	28.630
mp-1226003	CoPS	1.123	31.190	mp-1189150	Th(As ₃ O _s) ₄	0.466	41.001
mp-1317	CoSb ₃	0.163	31.824	mp-1179056	Th(BO _s) ₄	0.243	32.308
mp-1226296	CrCu(PSe ₃) ₂	0.640	27.964	mp-9619	Th(FeP ₃) ₄	0.535	38.004
mp-23116	CuBiSeO	0.301	31.968	mp-1208278	Th(P ₃ Ru) ₄	0.075	36.143
mp-927	CuP ₂	0.868	30.106	mp-382	Th ₃ As ₄	0.271	33.414
mp-20331	CuSbSe ₂	0.499	29.010	mp-23270	Th ₃ Bi ₄	0.092	31.759
mp-30452	DyNiBi	0.208	29.914	mp-1347	Th ₃ P ₄	0.262	29.339
mp-4510	DyNiSb	0.312	29.328	mp-552	Th ₃ Sb ₄	0.038	35.202
mp-1225491	DySbPd	0.230	28.246	mp-22786	ThNiSn	0.268	38.779
mp-16327	DySbPt	0.049	28.041	mp-10623	ThSbRh	0.744	34.373
mp-1212803	DyTeAs	0.329	30.294	mp-19886	ThSnPt	0.674	36.899
mp-1206712	ErNiBi	0.170	29.991	mp-3718	ThTeO	0.242	31.685
mp-21272	ErNiSb	0.274	29.580	mp-1217120	Ti ₂ FeNiSb ₂	0.941	35.129
mp-11836	ErSbPd	0.209	28.404	mp-998980	TiAlFeCo	0.125	36.827

Continued on next page

Continued from previous page

mp-5640	ErSnAu	0.006	29.391	mp-5967	TiCoSb	1.043	34.820
mp-1212634	ErTeAs	0.362	30.825	mp-866375	TiFe ₂ Ge	0.171	47.547
mp-21386	Eu(PIr) ₂	0.336	29.941	mp-866141	TiFe ₂ Si	0.402	43.603
mp-1095411	EuIn ₂ (GeIr) ₄	0.127	41.390	mp-19963	TiFe ₂ Sn	0.049	46.711
mp-9198	Fe(SiP) ₄	1.023	32.851	mp-961673	TiFeTe	0.985	35.642
mp-35596	Fe ₂ NiO ₄	1.362	28.153	mp-1008680	TiGePt	0.882	34.051
mp-19225	FeAgO ₂	1.148	28.932	mp-574169	TiGeTe ₆	0.337	36.452
mp-2008	FeAs ₂	0.283	43.455	mp-924130	TiNiSn	0.453	31.398
mp-561511	FeAsS	0.737	44.591	mp-20459	TiPbO ₃	1.813	29.328
mp-1101894	FeAsSe	0.449	47.376	mp-961682	TiSnPd	0.482	34.096
mp-1101938	2-Feb	0.515	40.344	mp-30847	TiSnPt	0.868	32.578
mp-1224908	FeNiSb ₆	0.128	33.806	mp-29711	Tl ₂ Te ₃	0.639	28.265
mp-1274279	FeO	1.816	30.190	mp-1239	Sb ₃ Ir	0.054	37.580
mp-20027	FeP ₂	0.433	45.520	mp-1219478	SbAsRh	0.539	37.103
mp-1101971	FePS	0.505	36.542	mp-8630	SbIrS	1.396	47.964
mp-1522	FeS ₂	0.877	28.015	mp-1095507	SbIrSe	1.147	50.175
mp-1224896	FeSb ₆ Pd	0.249	38.417	mp-1102833	SbOsS	1.119	35.894
mp-27904	FeSbS	0.547	44.702	mp-1101771	SbOsSe	1.123	37.484
mp-1103256	FeSbSe	0.622	47.452	mp-1103317	SbRhS	0.872	40.061
mp-1102580	FeSbTe	0.298	45.590	mp-1102366	SbRhSe	0.403	41.668
mp-760	FeSe ₂	0.374	32.860	mp-1103434	SbRuS	0.925	35.885
mp-871	FeSi	0.180	48.738	mp-1102395	SbRuSe	0.783	37.385
mp-19880	FeTe ₂	0.077	53.925	mp-1102430	SbTeIr	0.695	48.479

Continued on next page

Continued from previous page

mp-1102288	FeTeAs	0.682	49.792	mp-1103213	SbTeOs	0.858	40.618
mp-1072429	Ga ₂ Ru	0.127	37.377	mp-1219458	SbTeRh	0.552	43.280
mp-570844	Ga ₃ Os	0.677	32.340	mp-1102857	SbTeRu	0.627	41.492
mp-14791	Ge ₂ Te ₅ As ₂	0.409	36.101	mp-15661	Sc ₄ C ₃	0.329	29.023
mp-541312	Ge ₃ (Te ₃ As) ₂	0.343	36.303	mp-1219274	ScNb(NiSn) ₂	0.425	39.440
mp-9548	GeAs	0.511	32.173	mp-30459	ScNiBi	0.187	30.051
mp-1095275	GeP	0.489	32.531	mp-3432	ScNiSb	0.268	33.048
mp-1101755	GePtS	1.020	34.701	mp-569779	ScSbPd	0.016	32.624
mp-20817	GePtSe	0.660	36.222	mp-7173	ScSbPt	0.644	31.513
mp-938	GeTe	0.809	38.465	mp-2894	ScSnAu	0.122	31.638
mp-1224373	GeTePt	0.256	42.885	mp-1100405	ScTeRh	0.385	32.502
mp-1029330	Hf ₂ SeN ₂	0.607	29.039	mp-988	Si ₃ N ₄	4.250	29.466
mp-567817	HfGeTe ₄	0.331	35.332	mp-29157	Si ₃ P ₂ Pt	0.607	31.683
mp-924128	HfNiSn	0.387	33.746	mp-1206699	Si ₄ P ₄ Os	1.434	31.817
mp-1224358	HfSb ₄ Mo	0.139	40.430	mp-14983	Si ₄ P ₄ Ru	1.460	31.317
mp-866062	HfSiRu ₂	0.169	41.411	mp-2488	SiOs	0.512	46.524
mp-11869	HfSnPd	0.034	34.777	mp-1103261	SiPtSe	0.788	32.805
mp-1212255	Ho ₄ Ga ₁₂ Pt	0.219	27.898	mp-189	SiRu	0.230	46.453
mp-1018139	HoNiBi	0.194	30.141	mp-13305	SmSnAu	0.066	29.020
mp-4174	HoNiSb	0.292	29.461	mp-1208842	SmTeAs	0.380	29.450
mp-1212072	HoPPd	0.018	30.273	mp-38605	Sn(BiTe ₂) ₂	0.427	30.676
mp-30390	HoSnAu	0.022	29.527	mp-27947	Sn(SbTe ₂) ₂	0.253	37.274
mp-1077901	InCo ₃ SnS ₂	0.197	36.997	mp-1218953	SnGe ₄ Te ₄ Se	0.613	37.954

Continued on next page

Continued from previous page

mp-1223754	K(Nb ₃ Se ₄) ₂	0.391	30.122	mp-1218931	SnPtS	0.818	36.721
mp-18500	K ₃ Sn ₄ Au	0.397	38.674	mp-1218926	SnPtSe	0.574	38.511
mp-11132	KPrTe ₄	0.176	28.023	mp-691	SnSe	0.516	29.985
mp-1206717	LaBiPd	0.122	29.549	mp-1883	SnTe	0.042	40.639
mp-10288	LaCuTeS	0.577	28.022	mp-1218898	SnTePt	0.090	38.769
mp-1002107	LaRh	0.081	29.213	mp-15074	Sr(PIr) ₂	0.442	43.977
mp-550514	LaTa ₂ N ₂ O	0.671	29.423	mp-567278	Sr(Si ₃ N ₄) ₂	3.243	27.998
mp-989524	LaWN ₃	1.210	31.927	mp-9379	Sr(SnAs) ₂	0.009	29.791
mp-1222744	LaZnCuP ₂	0.186	28.513	mp-29662	TlBiSe ₂	0.232	27.943
mp-675779	Li ₂ Mo ₃ S ₄	1.437	29.217	mp-27438	TlBiTe ₂	0.468	29.432
mp-1029385	Li ₂ SnN ₂	1.697	34.949	mp-4573	TlSbTe ₂	0.127	33.736
mp-1185329	LiAcRh ₂	0.296	34.203	mp-568269	TmNiBi	0.149	29.278
mp-569450	LiB ₆ C	1.392	28.152	mp-4025	TmNiSb	0.255	29.330
mp-7936	LiNbS ₂	0.713	27.955	mp-1776	UN ₂	0.693	31.443
mp-1025496	LiNbSe ₂	0.732	28.673	mp-567636	VFeSb	0.349	41.101
mp-30457	LuNiBi	0.013	30.100	mp-30460	YNiBi	0.202	30.168
mp-20185	LuNiSb	0.215	31.174	mp-11520	YNiSb	0.295	29.581
mp-11917	Mg(BeN) ₂	4.066	32.452	mp-1207056	YSbPd	0.474	28.380
mp-865280	NbAlFe ₂	0.321	40.546	mp-4964	YSbPt	0.110	28.334
mp-1094088	NbCoSn	0.970	37.556	mp-4697	Zn(CrSe ₂) ₂	0.039	29.066
mp-9437	NbFeSb	0.514	40.147	mp-1215609	ZnGa ₁₁ Co ₄	0.240	32.307
mp-977410	NbGaFe ₂	0.091	41.533	mp-753	ZnSb	0.028	32.248
mp-9339	NbP	0.116	35.584	mp-1020712	ZnSiN ₂	3.194	30.130

Continued on next page

Continued from previous page

mp-1969	NbSb2	0.005	35.669	mp-11583	Zr2SN2	0.564	28.566
mp-505297	NbSbRu	0.377	38.616	mp-1079726	Zr2SeN2	0.337	30.393
mp-864954	MgMoN2	0.741	31.584	mp-1093991	ZrAsIr	0.269	37.090
mp-864908	MgTiIr2	0.013	42.230	mp-31451	ZrCoBi	0.977	35.696
mp-1104183	Mn(BiSe2)2	0.335	28.012	mp-1095610	ZrGePt	0.088	40.359
mp-18750	Mn(FeO2)2	0.998	28.400	mp-13542	ZrGeTe4	0.376	37.612
mp-569859	MnTl2SnTe4	0.310	28.657	mp-924129	ZrNiSn	0.495	35.101
mp-1221499	Mo2RuSe4	0.632	28.220	mp-1100415	ZrSbRh	1.165	36.074
mp-1634	MoSe2	1.301	30.583	mp-1183042	ZrSiRu2	0.235	42.829
mp-1008858	NdBiPd	0.105	30.821	mp-961687	ZrSnPd	0.482	35.931
mp-1206278	NdInCu4	0.005	33.139	mp-961713	ZrSnPt	0.963	34.645
mp-1206719	NdNiBi	0.512	30.028	mp-605	ZrTe5	0.019	33.901